FIRST-PRINCIPLES STUDY OF ONE-DIMENSIONAL ANTIMONY SELENIDE NANORIBBON

A Thesis

by

JAYBELLE DANNAH A. PRANADA

Submitted to the Office of Graduate and Professional Studies of
Texas A&M University
in partial fulfillment of the requirements for the degree of

MASTER OF SCIENCE

Chair of Committee,	Xiaofeng Qian
Committee Members,	Matt Pharr
	Qing Tu
Head of Department,	Ibrahim Karaman

August 2021

Major Subject: Materials Science and Engineering

ABSTRACT

The discovery of graphene and other 2D materials has led to extensive research on the effect of reduced dimensionality on the physical properties of van der Waals layered materials. In this thesis study, we explored the anisotropic nature of one-dimensional antimony selenide (Sb_2Se_3) nanoribbon. We investigated its electronic properties as well as strain-mediated modulation of their electronic properties. We performed a systematic study of atomic and electronic structure of Sb_2Se_3 bulk and nanoribbon using first-principles density functional theory. Elastic strain was found to have large impact on both atomic and electronic structure, which led to bandgap widening under small strain. Elastic strain also generated ripple formation and an indirect-to-direct band gap transition at large strain. The results demonstrated that it is possible to modify the band gap of ribbon-like chalcogenide materials via strain engineering, shedding light on potential straintronic applications. Furthermore, surface termination of bulk Sb_2Se_3 was studied and van der Waals surfaces were found to be the most stable ones. The results indicated the absence of dangling bonds at the surfaces of Sb_2Se_3 grains which is potentially beneficial to the photovoltaic performance.

DEDICATION

This thesis is dedicated to my family and friends, who never failed to support me.

ACKNOWLEDGMENTS

This thesis would not have been made possible for several people who reminded me that I can do this, that my hard work will eventually pay off in the end. First, I would like to thank my adviser, Dr. Qian, and my mentor, Baiyu, for teaching me DFT theory and guiding me through this research. I came from an experimental background so what I know about computational materials science is minimal. Thank you for the individual meetings and mentoring, not just for research but also life-lessons that I will always remember from now on.

To Baiyu, I am thankful for the long hours that you helped me understand the fundamentals and how to apply it in simulation packages. You always supported me in this research and eased my worries. Not only that, but you also provided friendship outside of being mentor-mentee, sharing your experiences and giving me career advice, and that is something that I am grateful of.

To the whole Materials Theory group, thank you for all the presentations you gave in the group meetings. I learned a lot on the versatility of computational materials science. To Nate, Hua, Alex and Daniel, thank you for giving me a leg up in DFT theory and continuously giving your suggestions. The introductory books truly helped me build the first bricks to my immersion in computational materials. To Xiuyu, thank you for helping me in research and classwork. It was nice when we sometimes sit down and just discuss the homework. The companionship, however short they may be due to the current state the world is in, was a small reprieve. Thank you everyone.

To my friends, both from the Philippines and here in the States, your chats at 2 am in the morning and weekend chats are a welcomed distraction. In the times I get too distracted with work, somehow you felt the stress 1,000 miles away and chatted me up to check on me. These small things helped me cope, made my will stronger to do better every day. To my colleagues at work and my supervisor, thank you for the daily companionship. Those small things like offering me coffee/energy drinks and asking how I was doing were a comfort to me. To Murat, thank you for checking up on me as often as you could and helping me in my career plans. To my family, my rock in trying times and the first to cheer in my triumphs, thank you. I cannot form the words to

thank you for the guidance, the support, and the love that I always receive from you. We may be miles apart but the love I feel for my parents, sisters, and relatives is a source of strength for me.

And lastly, to the Almighty Father, I sincerely thank You for all the blessings You have given me. In times of doubt, Your Words comforted me. Every time I do research, it always astounds me the way all things on this world was made and they remind me of Your omniscient presence. This thesis, this hard work of mine, and any work of mine in the future was and will be always offered to You, Lord.

I treasure these moments. I thank you for all the support and guidance. Wherever this road leads me, all the life-long lessons you have imparted on me has made its mark. From now on, I will do better and passionately succeed in my chosen path in materials science.

CONTRIBUTORS AND FUNDING SOURCES

Contributors

This work was supervised by a thesis committee consisting of Professor Xiaofeng Qian (advisor), Professor Qing Tu of the Department of Materials Science and Engineering, and Professor Matt Pharr of the Department of Mechanical Engineering. All the work conducted for the thesis was completed by the student independently.

Funding Sources

Theoretical calculations were carried out at the advanced computing resources provided by Texas A&M High Performance Research Computing.

NOMENCLATURE

1D	One-Dimensional
2D	Two-Dimensional
3D	Three-Dimensional
CBM	Conduction Band Minimum
DFT	Density Functional Theory
DOS	Density of States
GGA	Generalized Gradient Approximation
LDA	Local Density Approximation
NC PP	Norm Conserving Pseudopotential
PAW	Projector-Augmented Wave
PBE	Perdew-Burke-Ernzerhof
PDOS	Projected Density of States
PP	Pseudopotential
PZ	Perdew-Zunger
VBM	Valence Band Maximum

TABLE OF CONTENTS

Page

LIST OF FIGURES

FIGURE Page

LIST OF TABLES

TABLE Page

1. INTRODUCTION

1.1 Low-Dimensional Materials

In the recent two decades, the discovery of new materials has grown to the point of ubiquity in the modern scientific world. While tremendous effort has been exerted in efficiency optimization, the breakthrough of graphene in 2004, an allotrope of carbon made of a single layer of atoms in a two-dimensional (2D) honeycomb lattice [1], opened new studies on materials with reduced dimensionality. This led to the emergence of other 2D materials such as hexagonal boron nitride (h-BN) [2, 3], molybdenum disulfide (MoS_2) [4, 5, 6], and other transition metal chalcogenides, which expanded the understanding of 2D systems. As the dimensionality reduces, a few notable observations attracted attention. For example, bulk MoS_2 is known as an indirect semiconductor but when bulk MoS_2 is exfoliated down to a monolayer, its electronic band gap changes from indirect to direct, resulting in strong photoluminescence. Another example would be graphene which is a zero-gap semimetal but reducing its dimensionality can induce band gap opening, converting the semimetal material to a semiconductor [7]. Furthermore, few-layer graphene was found to sustain large elastic strain, the so-called *"smaller is stronger"* behavior. Besides mechanical properties, monolayer and few-layer graphene also exhibited remarkably high optical absorption, and electron mobility [1, 8, 9, 10]. These new discoveries led to new research in exploring how dimensionality can impact materials properties and how it can modulate these properties to fit different device applications.

Besides 2D materials, one-dimensional (1D) nanostructured materials have also gained some attention recently. An example is the graphene nanoribbon, long strips of planar layered graphene structure [8, 9]. A nonmagnetic graphene nanoribbon can be fabricated by cutting the ribbon with the armchair configuration along the ribbon edges. In contrast, cutting it with the zigzag edge passivated by hydrogen creates yields a wide-gap semiconductor ribbon [11]. Another example is the tunable band gap characteristics of 1D BN nanoribbons [3]. Thus, 1D materials showed

tunable electronic properties, making them an attractive material for semiconductor devices.

1.2 Tuning Electronic Properties via Strain Engineering

Elastic strain engineering offers a potential route to continuously fine-tune the electronic properties of materials by applying an elastic strain [3, 5]. In bulk materials, large elastic strain rarely exists since dislocations and plastic deformation can relax the elastic deformation. In materials with lower dimensionality, however, its size affects the relaxation of any deformation due to a higher surface-area-to-volume ratio ("smaller is stronger"). Minot et al. discovered the tunable band gap of carbon nanotubes by stretching the nanotube with the tip of an atomic force microscope (AFM) [12]. 2D MoS_2 monolayers can also sustain large strain and even undergo an optical band gap transition at 1% tensile strain [4, 13]. The electronic properties of 1D materials can also be on modulated by strain engineering, *e.g.*1D hexagonal BN (h-BN) nanoribbon exhibits tunable band gap under elastic strain [3] due to the confinement effect. Thus, using a 1D material with tunable electronic properties via elastic strain engineering is an attractive avenue that is worth exploring.

Although many 2D materials have been explored, research on 1D semiconducting nanostructures could be fruitful for both fundamental science and technological applications. Among these note-worthy materials are the 1D "van der Waals" chalcogenide materials, a special class of materials with a structure configuration of bundled ribbons held together by relatively weak van der Waals interactions [14, 15, 16, 17]. These include antimony chalcogenides (Sb_2S_3, Sb_2Se_3) and bismuth chalcogenides (Bi_2S_3, Bi_2Se_3) with space group #62 Pnma. Aside from their unique structure configuration, 1D "van der Waals" chalcogenide materials also garnered attention due to their attractive electronic and optical properties. Antimony selenide (Sb_2Se_3) is a compound with an orthorhombic crystal structure which has covalently-bonded ribbon structures and weak van der Waals interaction between adjacent ribbons [15, 16, 17, 18]. In addition to its unique structure configuration, Sb_2Se_3 has been used in electronic devices such as photovoltaics and photoelectrochemical applications [19, 17], which serves as a motivation for further exploration in modulating their intrinsic electronic properties for better device performance. Understanding the anisotropic

nature of 1D Sb_2Se_3 nanoribbon and exploring the possibility of tuning its electronic properties using strain engineering may shed light on the possibilities of tunable band gap applications of 1D semiconductors in the future. Compared to carbon nanotube, these 1D nanostructures are inherently semiconducting, and do not have other metallic/semimetallic variants like carbon nanotubes, making fabrication and processing simpler.

2. FIRST-PRINCIPLES DENSITY FUNCTIONAL THEORY

Physical and chemical properties of materials are fundamentally governed by the electronic and magnetic interactions of electrons and nuclei. With the advances in modern computers and high-performance computing clusters, one can model various materials, ranging from metals to semiconductors or from organic to inorganic materials, and study a wide range of physical and chemical properties using various computational approaches.

Different computational approaches have been developed to simulate the physical processes that take place at different length and time scale. Systems at the large length scale utilize finite element analysis while the Monte Carlo Method (MC) is often used for systems at the smaller scale to study thermodynamic and kinetic processes using statistical mechanics. On the other hand, Molecular Dynamics (MD) is often applied to study the dynamics of the system by computing atomic positions and forces and evolving the system based on Newton's laws. While classical MD can easily model systems with > tens of thousands of atoms for > tens of nanoseconds, classical MD requires accurate force fields to describe the interaction of atoms/ions. Construction of such force fields becomes challenging for materials under different physical, chemical, and mechanical environment, as the electrons, which are inherently playing a crucial role in the bond formation/breaking, cannot be easily and accurately considered. Moreover, the interactions between the electrons and the nuclei determine the electronic, optical, and magnetic properties of materials which cannot be directly described using classical MD.

Quantum mechanics-based approaches, *i.e.* first-principles methods or ab initio methods, were developed to directly take into account the subtle yet critical interactions between electrons and nuclei. Density functional theory (DFT) is one of the first-principles methods that have been developed and applied to successfully simulate electronic structure, thermodynamics, and kinetics of materials that were otherwise impossible to do with larger-scale methods.

For this paper, we will be focusing on first-principles methods to study the electronic properties of our material. A brief introduction to first-principles DFT is provided below.

2.1 The Many-Body Problem

The fundamental properties of particles can be described by the Schrödinger wave equation,

$$\hat{H}\Psi(r_i, R_I) = E\Psi(r_i, R_I)$$

where $\hat{H}$, Ψ, and E are the Hamiltonian operator, wave function, and eigen energy, respectively. $\Psi(r_i, R_I)$ depends on the positions of electrons r_i and nuclei R_I, thus it is difficult to solve or even store the wave functions for realistic systems with many electrons and nuclei. Approximations often need to be made while maintaining the accuracy. First, the large mass difference between the electron and the nucleus leads to the widely used Born-Oppenheimer approximation where the motions of electrons and nuclei are treated separately. Second, the time-dependence of the equation can be removed if only the ground state energy of the electrons is considered. Thus, the wave function of a molecule can be split into two separate terms: the electronic wave function and the nuclei wave function, solving the electronic wave function with r as the electronic coordinate:

$$\hat{H}(r)\Psi(r) = E\Psi(r)$$

The Hamiltonian $\hat{H}$ is a sum of all the energy contributions in the system: the kinetic energy of the nuclei E_I^{kin}, kinetic energy of the electrons E_i^{kin}, and the potential energies from the Coulombic interactions of electron-nucleus U_{iI}, electron-electron U_{ij} and the nucleus-nucleus U_{IJ}. For a given set of nuclei coordinates r_{iI}, the electronic Hamiltonian $\hat{H}_e$ only depends on three terms,

$$\hat{H}_e = E_i^{kin} + U_{iI} + U_{ij}$$

The kinetic energy operator of N_e number of electrons E_i^{kin} is defined as,

$$E_i^{kin} = -\frac{\hbar^2}{2m}\sum_i^{N_e}\nabla_i^2 = -\frac{1}{2}\sum_i^{N_e}\nabla_i^2$$

where ∇_i^2 is the Laplacian operator with respect to each independent variable in the coordinate system. The attractive potential energy operator between N_e electrons and *N* nuclei is defined as,

$$U_{iI} = -\sum_I^N\sum_i^{N_e}\frac{Z_I}{|r_i - R_I|}$$

where Z_I are the net charges of the nuclei, *N* and N_e are the number of nuclei and electrons present in the system, and r_i and R_I are the coordinates of the i^{th} electron and the I^{th} nucleus, respectively. The final energy describing the repulsive potential energies for N_e number of electron-electron interactions U_{ij} is defined as,

$$U_{ij} = \frac{1}{2}\sum_{i\neq j}^{N_e}\frac{1}{|r_i - r_j|}$$

where r_i and r_j are the coordinates of the i^{th} and j^{th} electron in the system. Summing the three energy operators, the Schrödinger equation is expanded as,

$$[-\frac{1}{2}\sum_i^{N_e}\nabla_i^2 - \sum_I^N\sum_i^{N_e}\frac{Z_I}{|r_i - R_I|} + \frac{1}{2}\sum_{i\neq j}^{N_e}\frac{1}{|r_i - r_j|}]\Psi(r) = E\Psi(r)$$

The equation above will serve as the starting point to calculate the ground state properties of a system using the obtained complex-valued wave function $\Psi(r)$. But the Schrödinger equation becomes a computationally expensive many-body problem as the system increases in size due to the number of wave functions required to solve the equation. This thesis relies on the fundamentals of density functional theory, where the ground state of the system has a unique ground state electronic density. Thus, both can be determined via a variational approach. The next sections focus on the

theorems, equations, and parameters to consider in the practical calculations of density functional theory.

2.2 Hartree-Fock Approach

Several theories were proposed to circumvent the many-body problem. Hartree devised an approach to the many-body problem called the one-electron model where the system is composed of a set of single electrons treated one at a time and only accounting the kinetic energy contribution, the electron-nuclei interaction, and the electrostatic potential between each electron and the average charge density of electrons known as the Hartree potential V_H.

$$[-\frac{1}{2}\sum_{i}^{N_e}\nabla_i^2 + U_{iI} + V_H]\psi(r) = E\psi(r)$$

The most important assumption considered is that the electrons are non-interacting and that the electron density $\rho(r)$ is simply the sum of the density from all the non-interacting orbitals. The wave function can be approximated by calculating the product of all the one-electron wave functions. Fock further improved the one-electron model by proposing that approximation of one-electron wave functions in the form of a Slater determinant. The anti-symmetry principle from identical particles was also satisfied by adding E_X, the exchange energy, which comes from the antisymmetric nature of the wave function in the Slater determinant form.

$$\hat{H}_{HF} = E_i^{kin} + U_{iI} + V_H + E_X$$

Hartree-Fock theory can be efficiently solved by utilizing nonlinear, self-consistent method of iteration.

2.3 Thomas-Fermi model

One of the first models in solving the electronic structure of many-body systems was formulated by Thomas and Fermi. The Thomas-Fermi model proposed that the wave equation of an

inhomogeneous electron gas can be solved by using the electronic density alone.

$$T_{TF}[\rho(r)] = \int \frac{3\hbar^2}{10m}(\frac{3}{8\pi})^{\frac{2}{3}}(\frac{dN}{dV})^{\frac{5}{3}}dV = C_{kin}\int \rho dV = C_{kin}\int \rho(r)d^3r$$

where T_{TF} is the kinetic energy term and $\rho(r)$ is the electron density. The energy functional still has the same energy contributions, except that the kinetic energy term can be expressed from the electron density.

$$E_{TF}[\rho(r)] = T_{TF}[\rho(r)] + V_{ext}(r) + V_H$$

The Thomas-Fermi model was found to be inaccurate due to missing crucial energy contributions, nevertheless it paved the important pathway towards density functional theory established by Hohenberg, Kohn, and Sham [20, 21].

2.4 Hohenberg-Kohn Theorems

The Hohenberg-Kohn theorems [21] established the solid connections among the electron density, external energy, Hamiltonian, and the wave function. The first theorem states that there exists a unique external potential V_{ext} determined by the ground state electron density. Once V_{ext} is determined, then so is the ground state electron density. The second theorem answers how to calculate for V_{ext} by showing the direct relationship between V_{ext} and the electron density. Hohenberg-Kohn theorized that the ground state wave function can be obtained variationally, where the electron density is successively varied at each iteration step, minimizing the energy until we reach the ground state of the Hamiltonian.

From the Thomas-Fermi model, V_{ext} is system-dependent, unlike the electronic kinetic energy and the potential from the electron-electron interaction, both of which are system-independent internal potentials. The ground state energy functional E[$\rho(r)$] is written as,

$$E[\rho(r)] = F[\rho(r)] + \int V_{ext}(r)\rho(r)dr$$

where the universal functional $F[\rho(r)]$ determines the density-dependent potentials for all systems. Although the Hohenberg-Kohn theorem did not provide an explicit formula for $F[\rho(r)]$, their conclusion is profound: the knowledge of the ground state electron density at a given V_{ext} can define the Hamiltonian, the wave function, the total energy, and any system property at its ground state.

2.5 Kohn-Sham Approach

The universal energy functional $F[\rho(r)]$ plays a critical role in the practical application of Hohenberg-Kohn theorem. Kohn and Sham proposed an approach that used the electron density as the key variable by mapping the many-electron problem to many one-electron non-interacting problem [20]. The kinetic energy of the electron E_i^{kin} is then decomposed into a non-interacting term E_{kin}^{non} and an interacting term E_{kin}^{int}. There is also a new correlation energy from the kinetic energy interaction E_c^{int} added to $\hat{H}$ derived from the Hartree-Fock approach.

$$\hat{H} = E_{kin}^{int} + E_{kin}^{non} + E_{ext} + E_H + E_X + E_c^{int}$$

The interacting terms can be grouped under one umbrella, the exchange-correlation energy E_{XC}, which represents the correlated energies coming from the interacting electronic systems, E_{kin}^{int} and E_c^{int}, and the exchange energy E_X, to account for the remaining energy contributions, that is,

$$E_{KS-DFT} = E_{kin}^{non} + E_{ext} + E_H + E_{XC}$$

The final form of E_{KS-DFT} consists of the non-interacting kinetic energy functional E_{kin}^{non} expressed with respect to the Kohn-Sham orbitals, the external energy functional E_{ext}, the Hartree energy functional E_H which accounts for the interaction between an electron at a specific electronic coordinate and the average electron density, and the exchange correlation energy functional E_{XC} which does not have an exact form but can be approximated.

2.6 Exchange-Correlation Energy Functionals

The last term in the Kohn-Sham Hamiltonian accounts for the remaining quantum effects not included in the other energy terms. The exchange correlation functional E_{XC} has two main contributions: the exchange energy between electrons with the same spin and the correlation energy between electrons with a different spin. The antisymmetric nature of the wave function from Pauli's exclusion principle requires that no two electrons with identical spins occupy the same orbital. This causes a separation between these identical electrons as they must occupy different and distinct orthogonal orbitals without any self-interaction.

The exchange energy E_X describes the interaction between the exchange hole left after the separation and the electron density. On the other hand, the correlation energy from interacting systems E_c^{int} is concerned with having two electrons with different spins occupying the same orbital. The two electrons also repel each other due to their Coulomb interaction, forming the correlation hole. Together with the exchange hole, they form the exchange-correlation hole XC. These two energy contributions in the total energy are important to solve as we consider how the electrons interact with each other. The concept of XC holes become the basis for the exchange-correlation functionals E_{XC} of DFT. Various approximations have been proposed over the years to improve the accuracy, including three types of widely used E_{XC} functionals: the local density approximation (LDA), the generalized gradient approximation (GGA), and the hybrid functionals.

Kohn and Sham's model theorized that E_{XC} can be approximated by considering a complex system is composed of homogeneous (or uniform) electron densities. LDA functional includes the sum of the energies from each electron:

$$E_{XC}^{LDA}[\rho(r)] = \int \rho(r)\epsilon_{XC}^{hom}[\rho(r)]dr$$

where $\epsilon_{XC}^{hom}[\rho(r)]$ is the exchange-correlation of a homogenous electron gas. The LDA works well for systems with such slow varying electron densities [22].

The GGA functional improves E_{XC} by considering both the local and semi-local terms from

the local electron density $\rho(r)$ and the gradient of electron densities, $\nabla\rho(r)$. There are several GGA functionals present today, such as Perdew-Burke-Ernzerhof [23] generalized gradient approximation (PBE).

$$E_{XC}^{GGA}[\rho(r)] = \int \rho(r)\epsilon_{XC}^{GGA}[\rho(r), \nabla\rho(r)]dr$$

Hybrid functionals include additional corrections, *e.g.* exact exchange, that are more computationally expensive to calculate compare to LDA and GGA in E_{KS-DFT}. In this thesis, the GGA-PBE functional is used to balance the accuracy and computational cost, although hybrid functionals may yield better band gap.

2.7 London Dispersion for Weak van der Waals Interaction

While the above GGA, LDA, and hybrid functionals work nicely for most materials, these approximations fail in describing the dispersive van der Waals (vdW) forces that arise from the induced dipole moments from fluctuating electron densities. An effective and robust scheme to account for long-range dispersive forces was proposed by Grimme et al. [24, 25, 26], where a dispersion correction is added to a semi-empirical GGA functional. The correction model was taken from London's formula expressing the energy from induced dipole interactions,

$$V(r) = \frac{C}{r^6}$$

where *C* is a parameter proportional to the polarizability volume and ionization energy of molecules, and *r* is the distance between atoms. It describes pairwise dispersion in the total energy,

$$E_{DFT-D} = E_{KS-DFT} + E_{disp}$$

where E_{KS-DFT} is the sum of all the energy contributions in the self-consistent KS energy. The term E_{disp} is the added dispersion correction, as shown in the equation below:

$$E_{disp} = -s_6 \sum_{i=1}^{N_{at}-1} \sum_{j=i+1}^{N_{at}} \frac{C_6^{ij}}{R_{ij}^6} f_{dmp}(R_{ij})$$

where N_{at} is number of atoms in the system, s_6 is a functional-dependent scaling factor, and R_{ij}^6 is the interatomic distance between atomic pair *ij*. The vdW correction term is particularly important for low-dimensional materials such as quasi-one dimensional antimony chalcogenides Sb_2X_3 which are composed of covalently bonded ribbon structures and vdW forces between adjacent ribbons.

3. PARAMETER VALIDATION FOR DFT CALCULATIONS

3.1 DFT Pseudopotentials

Core electrons in the inner shells are close to the nucleus, hence the interaction between the core electrons and electrons from different atoms is screened by the strong Coulombic potential from the nucleus. Meanwhile, all-electron (AE) wave function Ψ_{AE} of the core electrons contains multiple nodes which makes the calculation particularly expensive [27]. Pseudopotentials (PPs) were introduced in DFT to only consider valence electrons by pseudizing or "softening" the wave functions via the frozen-core approximation [28]. The pseudo wave functions Ψ_{PS} are constructed to replace Ψ_{AE} by removing the core part and only describing the outermost electron wavefunction with a much smoother wave function.

Several types of pseudopotentials have been developed in the past. Three main PPs are: norm-conserving pseudopotentials (NC PPs) [29], ultrasoft pseudopotentials (US PPs) [30], and projector-augmented wave (PAW) method [31]. NC PPs maintain that the integral of the squared amplitude of the pseudo wave functions inside the cutoff radius,

$$\int_{r \leq r_c} |\Psi_{PS}|^2 d^3r = \int_{r \leq r_c} |\Psi_{AE}|^2 d^3r$$

while PAW and US PPs significantly reduced the computational cost by relaxing the norm conserving constrains.

3.1.1 Selection of Pseudopotentials for Benchmark Calculations

Our theoretical studies are mainly based on first-principles DFT as implemented in the QUANTUM ESPRESSO [32, 33, 34] first-principles simulation package. We tested several pseudopotentials available in Quantum ESPRESSO to assess their accuracy for our system. There are many pseudopotential libraries in the package, but we chose specific pseudopotentials used in the majority of DFT studies on antimony chalcogenide systems [14, 15, 17, 18, 35, 36, 37, 38]. The bench-

Table 3.1: Benchmark studies of different pseudopotentials for calculating equilibrium lattice parameters a, b, and c.

Error in lattice constant (%)			**This Work**			Experiment (ICSD)[44]			Theory (Guo, GGA-PAW+vdW)[17]		
XC Functional	Pseudopotential Type	vdW Type	a	b	c	a = 11.794	b = 11.648	c = 3.986	a = 11.870	b = 11.482	c = 4.014
LDA	NC	none	11.665	11.302	3.982	-1.09	-2.97	-0.10	-1.72	-1.57	-0.80
GGA-PBE	PAW	none	12.887	11.511	4.025	9.26	-1.18	0.98	8.56	0.25	0.28
GGA-PBE	NC	none	12.826	11.503	4.025	8.75	-1.25	0.97	8.05	0.18	0.27
LDA	NC	DFT-D2	11.441	11.142	3.953	-3.00	-4.34	-0.82	-3.62	-2.96	-1.51
GGA-PBE	PAW	DFT-D2	11.992	11.429	3.995	**1.68**	**-1.88**	**0.22**	**1.03**	**-0.46**	**-0.48**
GGA-PBE	NC	DFT-D2	11.980	11.414	3.993	1.57	-2.01	0.19	0.92	-0.59	-0.51
LDA	NC	DFT-D3	11.665	11.302	3.982	-1.09	-2.97	-0.10	-1.72	-1.57	-0.80
GGA-PBE	PAW	DFT-D3	12.887	11.511	4.021	9.26	-1.18	0.87	8.56	0.25	0.16
GGA-PBE	NC	DFT-D3	12.826	11.503	4.025	8.75	-1.25	0.97	8.05	0.18	0.27

Percent error threshold: > 2% | 1% to 2% | < 1%

marks started with Troullier-Martins scalar relativistic pseudopotentials [39] with an exchange-correlation (XC) functional type of either the local density approximation (LDA-PZ) [22] or the generalized gradient approximation (GGA-PBE) [23]. We also included a van der Waals (vdW) correction term and compared their accuracy. We tried two primary vdW correction schemes in the QUANTUM ESPRESSO package: the original Grimme's DFT-D2 [24, 25] parametrization for all pairs of atoms and the more recent Grimme's DFT-D3 [40, 26] for three-body effects. Both were included as semiempirical addition of dispersive interaction to LDA/GGAfunctional.

3.1.2 Comparison of Equilibrium Lattice Constants

The LDA-PZ approximation led to an underestimation of lattice parameters compared to the experimental lattice parameters, as shown in Table 3.1. For reference, Table 3.2 and Table 3.3 also include other theoretical [14, 17, 35, 38] and experimental results [41, 42, 43, 44] that we used for further benchmarking of equilibrium lattice parameters. The addition of vdW corrections DFT-D2 and DFT-D3 obtained similar underestimation results with bare LDA-PZ functionals, which can be

Table 3.2: Benchmark studies of pseudopotentials for equilibrium lattice constants compared to the reported theoretical results.

Error in lattice constant (%)			This Work			Theoretical (GGA-PAW)[35]			Theoretical (LDA-PZ)[14]			Theoretical (HSE+D3)[38]		
XC Functional	Pseudopotential Type	vdW Type	a	b	c	a 11.910	b 11.700	c 3.980	a 11.520	b 11.220	c 3.960	a 11.520	b 11.912	c 3.799
LDA-PZ	NC	none	11.665	11.302	3.982	-2.05%	-3.40%	0.05%	1.26%	0.73%	0.55%	1.26%	-5.11%	4.79%
GGA-PBE	PAW	none	12.887	11.511	4.025	8.20%	-1.62%	1.13%	11.86%	2.59%	1.13%	11.86%	-3.35%	5.92%
GGA-PBE	NC	none	12.826	11.503	4.025	7.69%	-1.69%	1.12%	11.33%	2.52%	1.12%	11.33%	-3.42%	5.91%
LDA-PZ	NC	DFT-D2	11.441	11.142	3.953	-3.94%	-4.77%	-0.67%	-0.69%	-0.69%	-0.67%	-0.69%	-6.44%	4.04%
GGA-PBE	PAW	DFT-D2	11.992	11.429	3.995	0.69%	-2.32%	0.37%	4.09%	1.86%	0.37%	4.09%	-4.04%	5.13%
GGA-PBE	NC	DFT-D2	11.980	11.414	3.993	0.58%	-2.44%	0.34%	3.99%	1.73%	0.34%	3.99%	-4.16%	5.09%
LDA-PZ	NC	DFT-D3	11.665	11.302	3.982	-2.05%	-3.40%	0.05%	1.26%	0.73%	0.05%	1.26%	-5.11%	4.79%
GGA-PBE	PAW	DFT-D3	12.887	11.511	4.021	8.20%	-1.62%	1.02%	11.86%	2.59%	1.02%	11.86%	-3.35%	5.80%
GGA-PBE	NC	DFT-D3	12.826	11.503	4.025	7.69%	-1.69%	1.12%	11.33%	2.52%	1.12%	11.33%	-3.42%	5.91%

accounted towards the inaccuracy of employing LDA approximation to describe bulk Sb_2Se_3. With GGA-PBE, our lattice parameters were more comparable with other theoretical and experimental results for both PAW and NC PPs. For most of the employed functionals and pseudopotentials, we achieved a small error (error $< \pm 1\%$) in the c lattice parameter (along the ribbon direction).

However, the deviation in the direction transverse to the ribbon direction (a and b lattice parameters) reached up to a value of $\pm 9\%$ error with respect to experimental and theoretical findings. We accounted this huge margin to the large underestimation of non-negligible vdW contribution between adjacent and stacked 1D $(Sb_4Se_6)_n$ ribbons in bulk Sb_2Se_3. We tested the vdW correction for each functional and pseudopotential. With the GGA-PBE functionals and vdW correction, DFT-D2 showed more accurate results, with lattice parameters below $\pm 2\%$ error, giving a better description of the geometry within the GGA functional. Regarding pseudopotentials, both PAW and NC PPs have comparable lattice parameters, however NC PPs was more computationally expensive than PAW due to the required higher cutoff energy. Thus, we chose to use GGA-PBE exchange-correlation functional along with DFT-D2 vdW correction and PAW method for our DFT calculations.

Table 3.3: Benchmark studies of pseudopotentials for equilibrium lattice constants compared to the reported experimental results.

Error in lattice constant (%)			This Work			Experiment (Hurych)[43]			Experiment (Zheng)[42]			Experiment (El-Sayad)[41]		
XC Functional	Pseudopotential Type	vdW Type	a	b	c	a 11.770	b 11.620	c 3.960	a 11.780	b 11.630	c 3.990	a 11.790	b 11.640	c 3.980
LDA-PZ	NC	none	11.665	11.302	3.982	-0.89	-2.74	0.55	-0.97	-2.82	-0.20	-1.06	-2.90	0.05
GGA-PBE	PAW	none	12.887	11.511	4.025	9.49	-0.94	1.64	9.39	-1.02	0.88	9.30	-1.11	1.13
GGA-PBE	NC	none	12.826	11.503	4.025	8.97	-1.01	1.63	8.88	-1.09	0.87	8.78	-1.18	1.12
LDA-PZ	NC	DFT-D2	11.441	11.142	3.953	-2.80	-4.11	-0.17	-2.88	-4.19	-0.92	-2.96	-4.27	-0.67
GGA-PBE	PAW	DFT-D2	11.992	11.429	3.995	1.88	-1.64	0.88	1.80	-1.73	0.12	1.71	-1.81	0.37
GGA-PBE	NC	DFT-D2	11.980	11.414	3.993	1.78	-1.77	0.84	1.69	-1.86	0.09	1.61	-1.94	0.34
LDA-PZ	NC	DFT-D3	11.665	11.302	3.982	-0.89	-2.74	0.55	-0.97	-2.82	-0.20	-1.06	-2.90	0.05
GGA-PBE	PAW	DFT-D3	12.887	11.511	4.021	9.49	-0.94	1.53	9.39	-1.02	0.76	9.30	-1.11	1.02
GGA-PBE	NC	DFT-D3	12.826	11.503	4.025	8.97	-1.01	1.63	8.88	-1.09	0.87	8.78	-1.18	1.12

3.2 Optimization of DFT Parameters

3.2.1 Supercells and Periodic Boundary Condition

DFT codes such as Quantum ESPRESSO often adopt the periodic boundary condition to simulate the periodic bulk materials. For crystals, this becomes advantageous since atoms in solids are periodically arranged in repeating unit cells. From Bloch's theorem, the solution to DFT KS equation in a periodic potential leads to the KS eigen wavefunction ψ_{nk}, which is a product of a plane wave, $e^{ik\cdot r}$, and a cell-periodic part, $u_n(r)$,

$$\psi_{nk}(r) = e^{ik\cdot r}u_n(r)$$

where $u_n(r) = u_n(r+R)$, *r* is the position, and *R* is lattice vector. Using Fourier theorem, the cell-periodic function $u_n(r)$ can be expanded in plane waves *G*,

$$u_{nk}(r) = \sum_G c_{nk}(G)e^{iG\cdot r}$$

Using $u_k(r)$, we can express the wave function ψ_{nk} as the sum of plane waves:

$$\psi_{nk}(r) = \sum_G c_{nk}(G) e^{i(k+G)\cdot r}$$

In principle, the wave function at each k-point would need to be expanded in an infinite number of plane waves. However, in practice, we choose a finite cutoff for the planewave basis to balance the accuracy and efficiency. The energy cutoff E_{cut} sets the finite expansion, $\frac{1}{2}(|k+G|)^2 \leq E_{cut}$, neglecting higher energy terms in the Fourier expansion. As E_{cut} is system-dependent, it is necessary to do convergence tests on critical parameters including E_{cut} before any production calculations to ensure accurate results are obtained [20].

3.2.2 Convergence Tests

DFT calculations become computationally expensive if the chosen parameters are not optimized. Ground state calculation is performed through an iterative process where it starts with an initial trial wave function, calculates the corresponding kinetic energy and potential energy, and updates the wavefunction. This process is continuously repeated until the total energy of the system converges within the set convergence threshold [45]. Thus, convergence tests on the plane-wave energy cutoff and k-point sampling need be done to speed up the convergence of the self-consistent calculations while achieving the desired accuracy.

Before structural optimization and further calculations, convergence tests were performed on the plane-wave cutoff energy for bulk Sb_2Se_3, and k-point sampling and vacuum convergence for 1D $(Sb_4Se_6)_n$ nanoribbon. For bulk Sb_2Se_3 we selected the energy cutoff range from 30 – 100 Rydberg (Ry), shown in Figure 3.1 (a). The total energy dropped from 30 to 40 Ry and gradually converged from 60 to 100 Ry. The energy cutoff of 60 Ry was sufficient for self-consistent calculations to compensate for the increased computational cost along with larger cutoff. For 1D $(Sb_4Se_6)_n$ nanoribbon, we chose a smaller energy cutoff range from 15 to 60 Ry due to the reduced dimensionality. From Figure 3.1 (b), the total energy convergence was faster after a steep decline from 15 to 20 Ry. The energy cutoff of 25 Ry was the best choice for 1D $(Sb_4Se_6)_n$ nanoribbon to

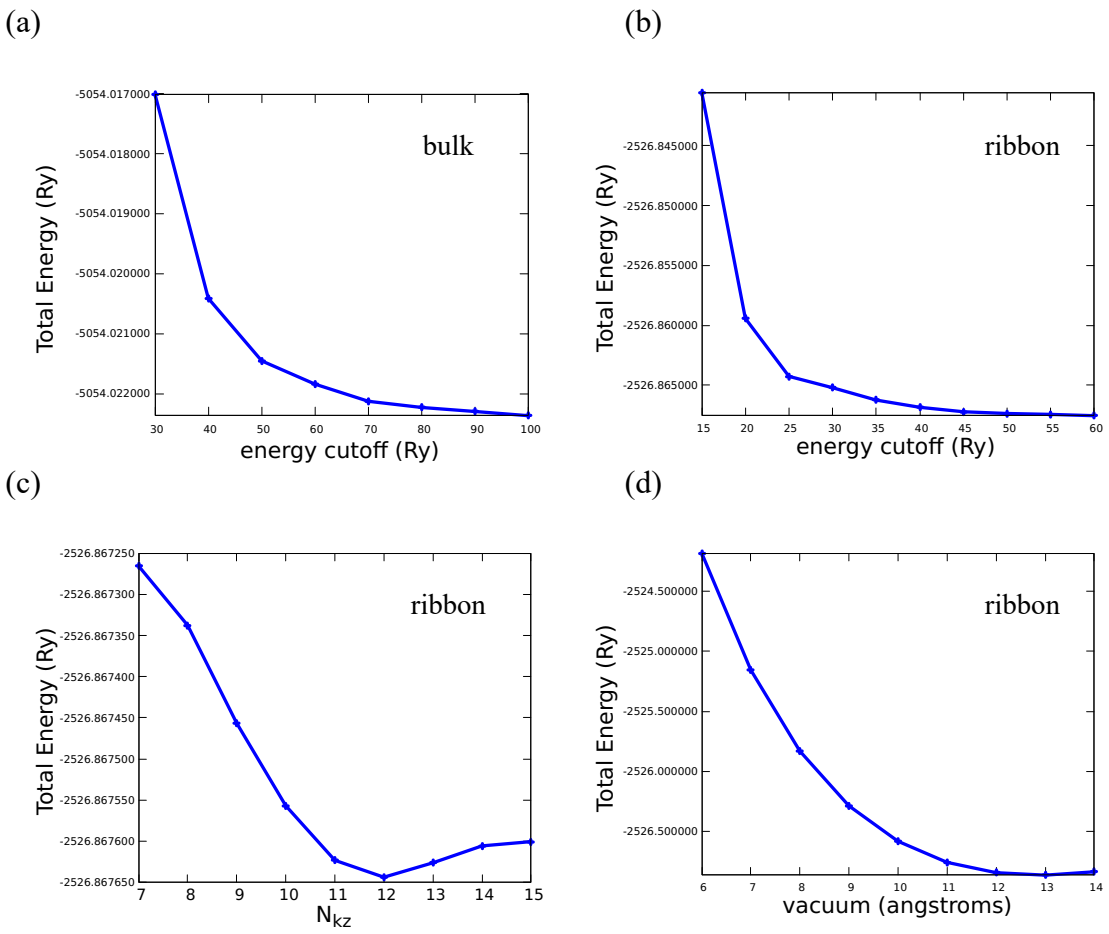

Figure 3.1: Convergence tests for the (a)—(b) plane-wave energy cutoff for bulk Sb_2Se_3 and $(Sb_4Se_6)_n$ ribbon, (c) k-point sampling for $(Sb_4Se_6)_n$ ribbon, and (d) vacuum thickness surrounding the $(Sb_4Se_6)_n$ ribbon.

achieve faster convergence and less computational cost.

K-point sampling was particularly important for 1D $(Sb_4Se_6)_n$ nanoribbon since the crystal structure is only periodic along the ribbon direction. It requires a large k-point sampling along *c*-direction, N_{kz}, and a minimum k-point sampling in the transverse directions N_{kx}=N_{ky}=1. We used N_{kz}=7 to 15 for k-point sampling along the ribbon direction. From Figure 3.1 (c), N_{kz}=12 was sufficient to adequately sample along the first Brillouin zone.

To minimize the periodic interaction between 1D $(Sb_4Se_6)_n$ nanoribbons, the vacuum thickness must also be optimized. The vacuum thickness along the *a*- and *b*- directions ranged from 6 to 14

Å, as shown in Figure 3.1 (d). The total energy gradually decreased and reached the convergence at a vacuum thickness of 13 Å.

3.3 Summary of Optimized Parameters

To optimize the computational cost and accuracy, we chose to use the GGA-PBE exchange correlation energy functional, the DFT-D2 vdW correction, and the PAW method for our DFT calculations. The optimized parameters from the convergence tests generated a set of parameters each for bulk Sb_2Se_3 and 1D $(Sb_4Se_6)_n$ nanoribbon. For the bulk structure, a plane-wave energy cutoff of 60 Ry (*i.e.*, 816 eV) is sufficient to reduce the basis set and quickly converge the total energy. For 1D $(Sb_4Se_6)_n$ nanoribbon, we chose a smaller energy cutoff of 25 Ry (*i.e.*, 340 eV) for balancing the accuracy and computational cost. In addition, a k-point mesh of 1x1x12 and a vacuum thickness of 13 Å were selected for the DFT calculations of 1D $(Sb_4Se_6)_n$ nanoribbon.

4. INTRINSIC PROPERTIES OF BULK ANTIMONY SELENIDE AND ANTIMONY SELENIDE NANORIBBONS

4.1 Bulk Antimony Selenide Crystal Structure

To optimize the geometry of bulk Sb_2Se_3 crystal structure, we performed DFT calculations using the QUANTUM ESPRESSO package within the Perdew-Burke-Ernzerhof generalized gradient approximation (GGA-PBE). We employed the projector augmented-wave (PAW) method to describe the electron-core interaction and the semiempirical Grimme's DFT-D2 vdW functional to account for the weak vdW interaction between neighboring 1D $(Sb_4Se_6)_n$ ribbons inside bulk Sb_2Se_3. The structural and electronic calculations used a plane-wave energy cutoff of 60 Ry (*i.e.*, 816 eV) and a Monkhorst-Pack k-point sampling grid of 6×6×18. We set a maximum residual force less than 0.02 eV/Å as the convergence criterion for geometry optimization, and 10^{-6} Ry for the electronic relaxation convergence criterion. Shown in Figure 4.1 (a)—(c) are the optimized crystal structure of bulk Sb_2Se_3, viewed in different perspectives.

4.2 One-Dimensional Antimony Selenide Nanoribbon

For 1D $(Sb_4Se_6)_n$ nanoribbon, we fully relaxed the structure without any symmetry constraints. An energy cutoff of 25 Ry was set for structural and electronic calculations with a k-point sampling grid of 1×1×12 in the Brillouin zone. Supercell was adjusted to have a sufficiently large separation (> 13 Å) along *a*- and *b*- directions to minimize the interaction between periodic images. Figure 4.1 (d)—(f) illustrates the addition of vacuum around the $(Sb_4Se_6)_n$ nanoribbon.

4.3 Band Structure Calculations

To understand the electronic properties of bulk Sb_2Se_3 and 1D $(Sb_4Se_6)_n$ nanoribbon, we calculated the band structure of bulk Sb_2Se_3 using GGA-PBE and DFT-D2 vdW correction, as plotted in Figure 4.2 (a). We selected our high-symmetry k-point path in the Brillouin zone using Materials Cloud [46, 47] and used XCrySDen for visualization [48]. Our calculations for bulk Sb_2Se_3 achieved an indirect gap of 0.79 eV and a direct gap of 0.82 eV. Both direct and indirect band gaps

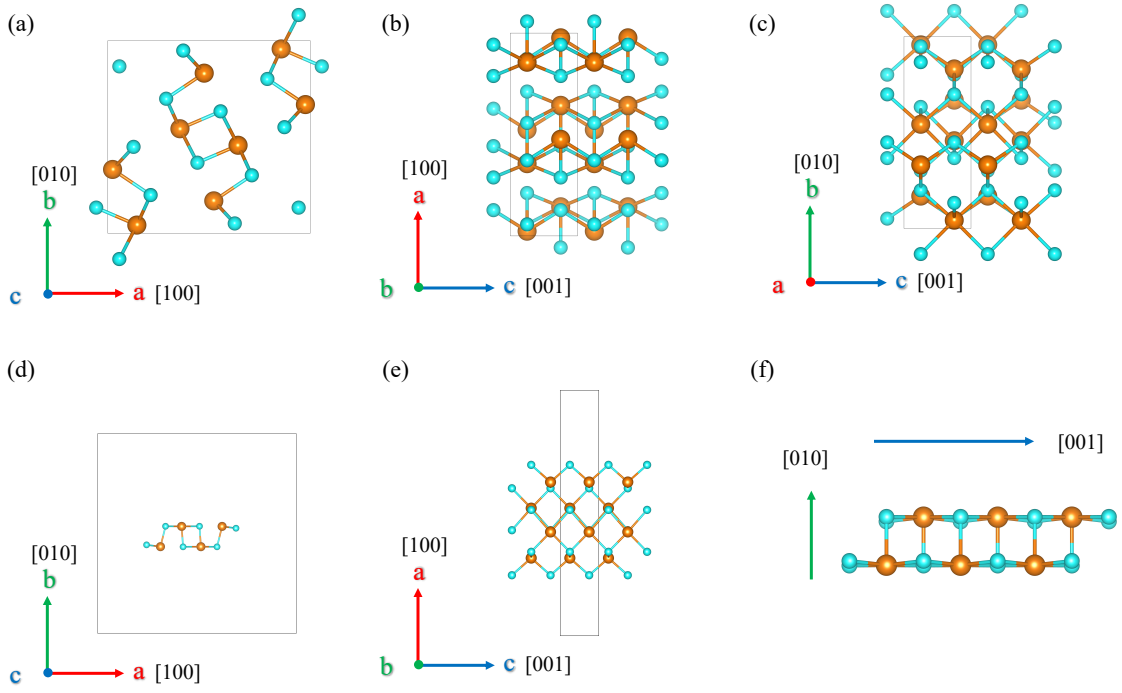

Figure 4.1: Crystal structure of bulk Sb_2Se_3 and 1D $(Sb_4Se_6)_n$ nanoribbon (a) Top view of bulk Sb_2Se_3 along [001] direction, (b) Side view of bulk Sb_2Se_3 along [010] direction, and (c) Side view of bulk Sb_2Se_3 along [100] direction. (d) 1D $(Sb_4Se_6)_n$ nanoribbon centered with vacuum added along [010] and [100] directions. (d) Top view along the ribbon direction, (e) Side view of 1D $(Sb_4Se_6)_n$ nanoribbon along [010] direction, and (f) A view of 1D $(Sb_4Se_6)_n$ nanoribbon along [001] direction. Sb: larger atom in orange, and Se: smaller atom in blue.

of bulk Sb_2Se_3 are relatively close to each other, which enables easy band gap transition. Both the valence band maximum (VBM) and the conduction band minimum (CBM) lie along the ΓY path with a small shift for band gap transition from direct to indirect (< 0.1 eV).

The results were in good agreement with previous theoretical works [14, 17] that also used the GGA functional, as shown in Table 4-1. However, we see that the bandgap values calculated are lower than the experimental values for bulk Sb_2Se_3. Band structure calculations are particularly sensitive to the selection of meta-GGA XC functionals, and the GGA functionals usually underestimate the bandgap for semiconductors and insulators. Although we observed a widening of bandgap for 1D $(Sb_4Se_6)_n$ nanoribbon from the GGA-PBE functionals, the true bandgap of 1D $(Sb_4Se_6)_n$ nanoribbon is expected to be higher than the current GGA values due to the reduced

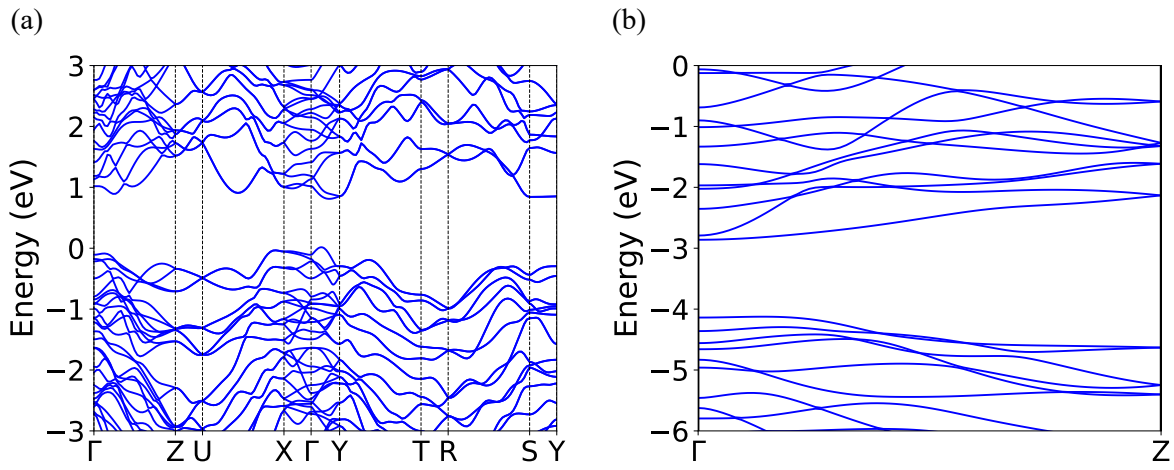

Figure 4.2: Band structure plot of (a) bulk Sb_2Se_3 and (b) 1D $(Sb_4Se_6)_n$ nanoribbon.

screening from the absence of interchain vdW interaction.

We calculated the band structure and dispersions along the ΓZ path, that is, along the ribbon direction. The band structure of 1D $(Sb_4Se_6)_n$ nanoribbon shown in Figure 4.2 (b) exhibit VBM and CBM lying near the high symmetry point Γ with a calculated indirect gap of 1.26 eV and a direct gap of 1.28 eV. It was also observed that the direct-indirect band gap transitions are relatively close to each other, with the indirect bandgap being slight greater with a narrow offset of 0.02 eV. We further calculated the change of band gap due to the addition of vdW correction, and we found that the band gaps with and without vdW correction remain close to each other. Meanwhile, without vdW correction, the 1D $(Sb_4Se_6)_n$ nanoribbon has an indirect gap of 1.26 eV and a slightly higher direct gap of 1.30 eV.

4.4 Density of States Calculations

To illustrate the electronic contribution of each chemical element, we plotted the projected density of states (PDOS) of bulk Sb_2Se_3 with the energy range of -10 eV to 5 eV with respect to the Fermi level. From the PDOS plot in Figure 4.3 (a), Se *s* orbitals dominated the deepest valence bands occurring between about -9 to -6 eV, while the valence bands closer to the valence band maximum (VBM) were mostly occupied by Sb *s* states. The conduction bands are dominated

Table 4.1: Band gap comparison between bulk Sb_2Se_3 and 1D $(Sb_4Se_6)_n$ nanoribbon.

Structure	Functional	E_g (direct), eV	E_g (indirect), eV
bulk	GGA - **This work**	0.8265	0.7948
	GGA+vdW - **This work**	0.8265	0.7948
ribbon	GGA - **This work**	1.2999	1.2640
	GGA+vdW - **This work**	1.2776	1.2635
bulk	Experimental	~ 1.2	~ 1.17
	Theory (GGA+vdW)	0.8036	0.8030
	Theory (DFT+MBJ)	1.2388	1.2236
	Theory (DFT+HSE06)	1.3469	1.3366

by both Se *p* and Sb *p* orbitals. For 1D $(Sb_4Se_6)_n$ nanoribbon in Figure 4.3 (b), we plotted the projected density of states (PDOS) with the energy range of -6 eV to 0 eV. The plot showed that the valence bands are dominated by both Sb *p* orbitals and Se *p* orbitals. Interestingly, the proportion of states at the conduction band minimum (CBM) are essentially dominated by Sb *p* orbitals. We tentatively account this to the more prominent quantum confinement effect of 1D $(Sb_4Se_6)_n$ nanoribbons compared to bulk Sb_2Se_3. In bulk Sb_2Se_3, the adjacent ribbons are held together by weak vdW interactions. Introducing a vacuum space around the ribbon to separate periodic images confines the wavefunctions, thereby increasing the band gap for 1D $(Sb_4Se_6)_n$ nanoribbon.

4.5 Cohesive Energy

4.5.1 Introduction

Investigating the cohesive energy of solids provides an overview of the interactions of the bulk material and its atomic species. The cohesive energy of a solid is referred to as the energy needed to break the materials into its constituent atoms. For ribbon-like transition metal chalcogenides such as Sb_2Se_3, we can separate the cohesive energy into two parts: $E_{coh,ribbon}$, which describes

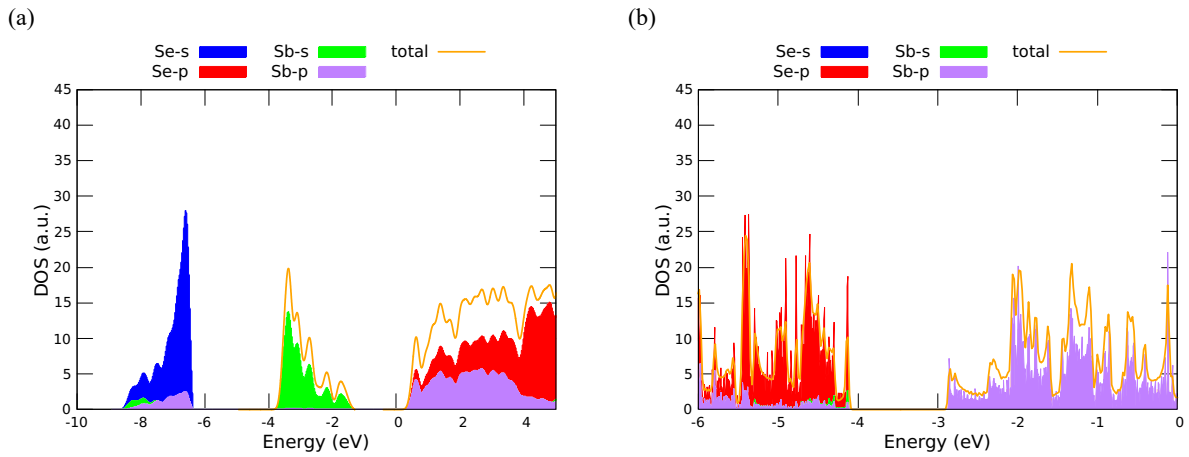

Figure 4.3: Projected density of states (PDOS) of (a) bulk Sb_2Se_3 and (b) 1D $(Sb_4Se_6)_n$ nanoribbon solved by DFT calculations.

the cohesiveness of the bonds keeping Sb and Se atoms together to form a single ribbon, and $E_{coh,bulk}$ which describes the cohesiveness of the ribbons keeping bulk Sb_2Se_3 together. $E_{coh,ribbon}$ is therefore defined as,

$$E_{coh,ribbon} = -(E_{Sb_4Se_6} - n_{Sb}E_{Sb} - n_{Se}E_{Se})/n_{atoms}$$

where $E_{Sb_4Se_6}$, E_{Sb}, and $E_{Se}$are the total energies of a single $(Sb_4Se_6)_n$ nanoribbon, bulk Sb per Sb atom, and bulk Se per Se atom, respectively. n_{Sb}, n_{Se}, and n_{atoms} are the number of Sb and Se atoms in a single $(Sb_4Se_6)_n$ nanoribbon, and n_{atoms} is the total number of atoms.

The cohesive energy calculation for bulk Sb_2Se_3 required a different approach. We can imagine extracting a ribbon from the bulk, and the energy required to cut through the bulk and keep adjacent ribbons infinitely separated away from each other is the corresponding $E_{coh,bulk}$. This is particularly important for ribbon-like structures such as Sb_2Se_3 where its anisotropic nature is described by the strong localized covalent bonding along the ribbon direction and the weak van der Waals interaction between the adjacent ribbons. With this bonding inhomogeneity in Sb_2Se_3, extracting a single $(Sb_4Se_6)_n$ nanoribbon from the bulk would require breaking the weak vdW bonds holding the ribbons together. $E_{coh,bulk}$ is described as the difference between the total energy of the unit

cell and the total energy of the isolated ribbons per unit area [14], which is written as:

$$E_{coh,bulk} = -(E_{total} - n_{ribbons}E_{ribbon})/A$$

where E_{total} is the total energy of the unit cell, E_{ribbon} is the total energy of an isolated single ribbon, and $n_{ribbons}$ are number of $(Sb_4Se_6)_n$ ribbons in each unit cell. In this case, $n_{ribbons}$ = 2.

4.5.2 Computation Approach

To calculate $E_{coh,bulk}$, we need to calculate the interfacial area between the adjacent ribbons dominated by vdW interaction. Here we consider the four side planes for the corresponding interfacial area. Two polygons were constructed, "boxing" one selected ribbon in each, by approximating the midpoint of the closest Sb-Se bonds and connecting the midpoints to draw the sides of the box, shown in Figure 4.4 (a). Shown in Figure 4.4 (a) and (b) are the estimated area around two adjacent ribbons near the center of the supercell, and a 3D projection of both areas.

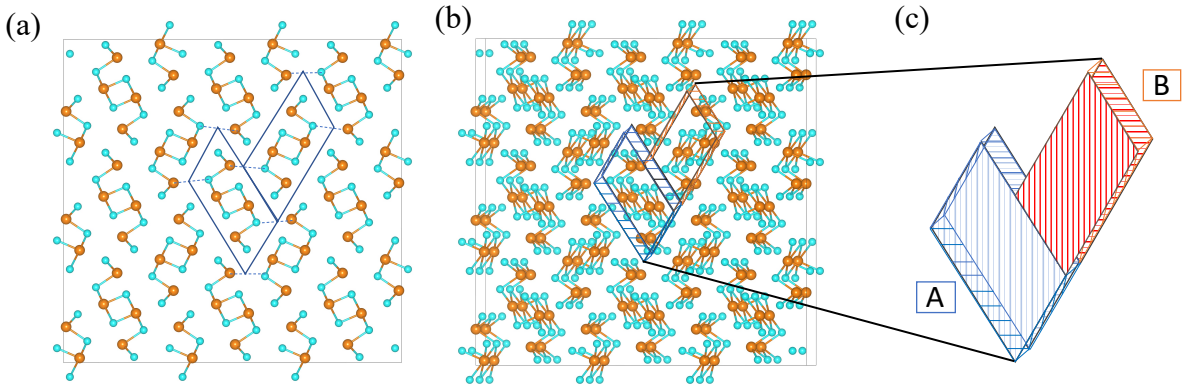

Figure 4.4: Interfacial area estimated around a ribbon. (a) Surfaces between adjacent ribbons in a 3x3x1 supercell configuration. (b) Tilted view of the supercell. (c) Interfacial polygons with shaded planes shown in a 3D perspective.

We then calculate the surface area of both boxes. The average surface area was calculated around 54 $Å^2$. We obtained $E_{coh,bulk}$ of 0.592 Jm^{-2}, which agreed with previous theoretical work

[15]. $E_{coh,ribbon}$ is larger, at 0.3 eV/atom, due to the stronger Sb-Se covalent bonding. Compared to the cohesive energy of graphite of 0.4 Jm^{-2}, $E_{coh,bulk}$ of 0.592 Jm^{-2} indicates that $(Sb_4Se_6)_n$ nanoribbons may be exfoliated from their bulk.

4.6 Conclusion

We calculated the band structure and density of states of bulk Sb_2Se_3 and 1D $(Sb_4Se_6)_n$ nanoribbon using GGA-PBE and DFT-D2 vdW correction. The DOS plots reflected the quantum confinement effect in 1D $(Sb_4Se_6)_n$ nanoribbon from the absence of interchain vdW interaction. The confinement effect in 1D $(Sb_4Se_6)_n$ nanoribbon induced a widening in band gap. The band structure and density of states calculations suggest that the use of GGA-PBE is sufficient to describe the intrinsic electronic properties of 1D $(Sb_4Se_6)_n$ nanoribbon for strain engineering calculations without using computationally-expensive hybrid exchange-correlation energy functionals. $E_{coh,bulk}$ is comparable to that of graphite, indicating that $(Sb_4Se_6)_n$ nanoribbons may be exfoliated from their bulk.

5. INVESTIGATION OF SURFACE TERMINATION ON BULK ANTIMONY SELENIDE STRUCTURE

5.1 Introduction

Surface termination often plays an important role in the performance of various devices, *e.g.* photovoltaics. Hence, understanding the stability of difference surfaces in antimony chalcogenides can help design materials processing and avoid detrimental dangling bonds at the surfaces, grain boundaries, etc. Sb_2Se_3 belongs to the ribbon-like chalcogenide family, where their structures contain strong covalently linked ribbons stacked together by weak vdW interactions [17]. This makes Sb_2Se_3 a highly anisotropic material, and the ribbons in Sb_2Se_3 have been proven efficient in charge transport. Established 2D layered materials such as graphene and GaSe also have strong structural anisotropy due to the weak vdW bonds between the 2D layers. However, the presence of quasi-dimensional ribbons in the bulk structure, as compared to graphene's sheet-like configuration, brings forth the question of the surface orientation when cleaving the bulk Sb_2Se_3 [38]. Mechanical exfoliation is easier along the weak vdW bonds, as reflected in the lower $E_{coh,bulk}$, but cutting a surface slab from the bulk structure may break the strong covalent bonds of the quasi-dimensional ribbons and introduce broken or dangling bonds. The unsatisfied valence bonds will introduce gap states within the semiconductor's band gap, thereby changing the performance of the materials. Hence, surface termination of bulk Sb_2Se_3 is worth exploring.

5.2 Surface Calculations

To study surface termination, we used the slab model which contains a bulk region sandwiched by two surfaces of interest. In practice, a supercell was created to represent an infinite 2D [49]. Sufficient vacuum was added to avoid the image interaction due to periodic boundary condition, that is, to remove any interaction between the two opposite surface terminations from adjacent slabs. We classified the selected slabs according to the ribbon orientation: (1) slab model with ribbon parallel to its surface, (2) slab model with ribbon tilted away from the surface.

5.2.1 Slab Model with Ribbons Parallel to the Slab

Shown in Figure 5.1 (a)—(f) are the unrelaxed and optimized (010), (120), and (420) slab planes in which the ribbon is parallel to the surface. All the surfaces were reconstructed after relaxation and have no disrupted Sb-Se covalent bonds. This is due to the flexibility of the structure to heal broken vdW bonds by adjusting the local coordinates to reduce the surface energy. We computed the surface energy of unrelaxed (010) surface to be 0.20 Jm^{-2}, while the fully optimized surface has a lower surface energy of 0.14 Jm^{-2}. The relatively small difference in the relaxation indicates the small surface reconstruction after relaxation. The surface energy for (120) and (420) planes also showed small change between the unrelaxed and the fully optimized surfaces. Our computed surface formation energies for (120) and (420) are as follows: 0.33 Jm^{-2} and 0.25 Jm^{-2} for the unrelaxed and optimized (120) plane, respectively; and 0.12 Jm^{-2} and 0.09 Jm^{-2} for the unrelaxed and optimized (420) surface, respectively.

We then compared the density of states (DOS) of the unrelaxed and relaxed surfaces with the bulk structure to analyze any changes in the electronic structure, particularly the distribution of states in the band gap region. In all DOS plots, the Fermi level is set to 0 eV for comparison. The DOS plots in Figure 5.2 (a) and (c) for (010) and (420) surfaces showed that there is little change in the band gap region before and after the relaxation, which is consistent with the minimal surface reconstruction on these two surfaces. In contrast, the (120) surface initially has significant DOS inside the band gap, and after relaxation, most DOS in the gap was removed by the reconstruction.

We further studied another two planes: (100) and (001) planes. Both surfaces cut through the strong Sb-Se covalent bonds of the ribbon and introduced dangling bonds in the new slab. Initially, the (100) surface in Figure 5.1 (g) and (h) showed periodic images for Se(1) and Se(2) atoms. The angled orientation of the ribbons in the bulk structure prevented a clean (100) cleaved surface. After structural optimization, there is significant relaxation on the surface. This is reflected in a higher surface energy for (100) slab: 0.38 Jm^{-2} for the unrelaxed surface and 0.18 Jm^{-2} for the fully optimized surface. The larger surface energy difference mostly comes from the surface reconstruction to heal dangling bonds. Similarly, the (001) surface also has high surface energies:

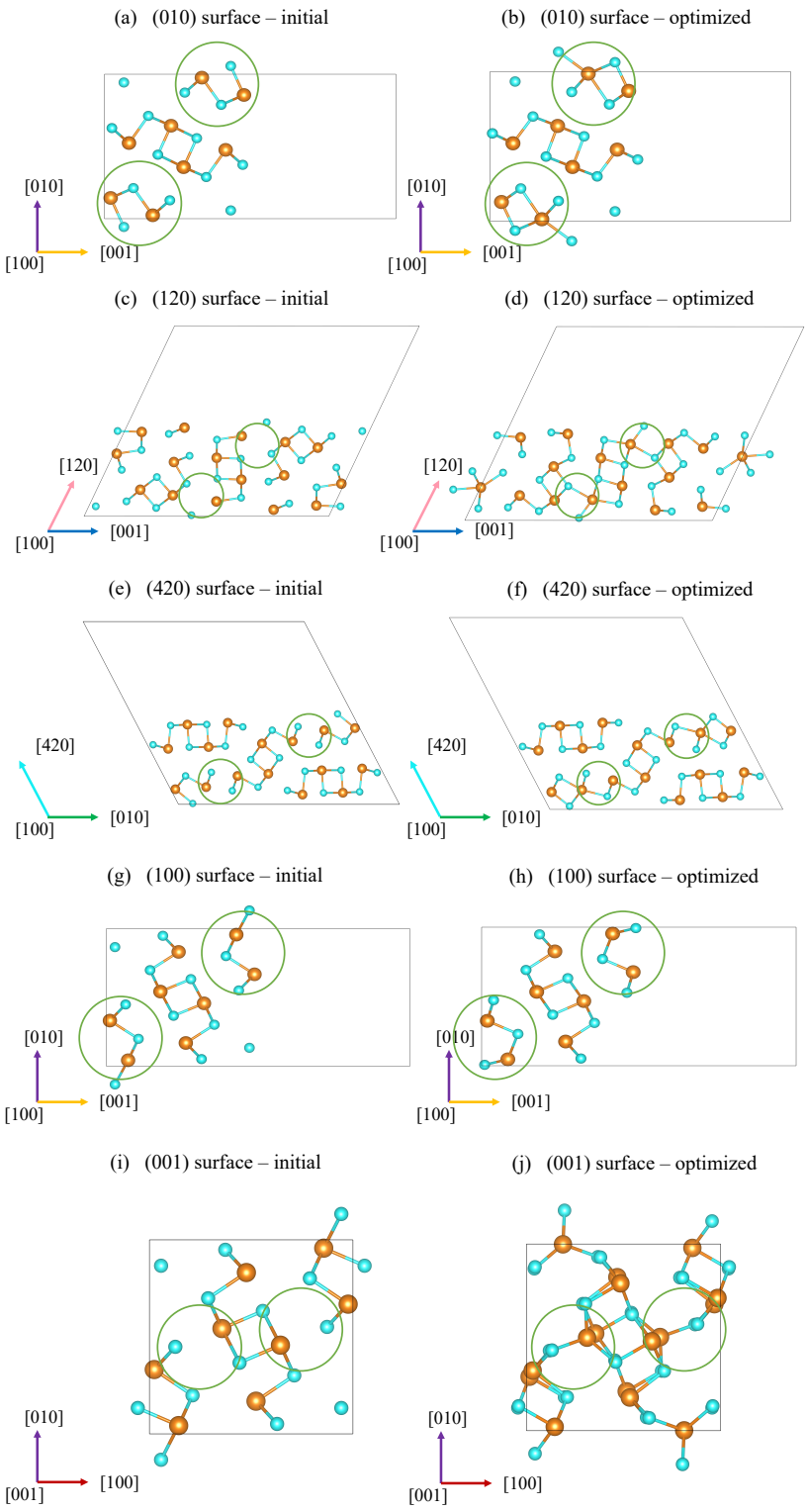

Figure 5.1: Unrelaxed and optimized slab structures of Sb_2Se_3 (a)—(b) (010) plane, (c)—(d) (120) plane, (e)—(f) (420) plane, (g)—(h) (100) plane, and (i)—(j) (001) plane. Green circles highlight surface reconstruction by healing of broken bonds or formation of new bonds. Sb: larger atom in orange, Se: smaller atom in blue.

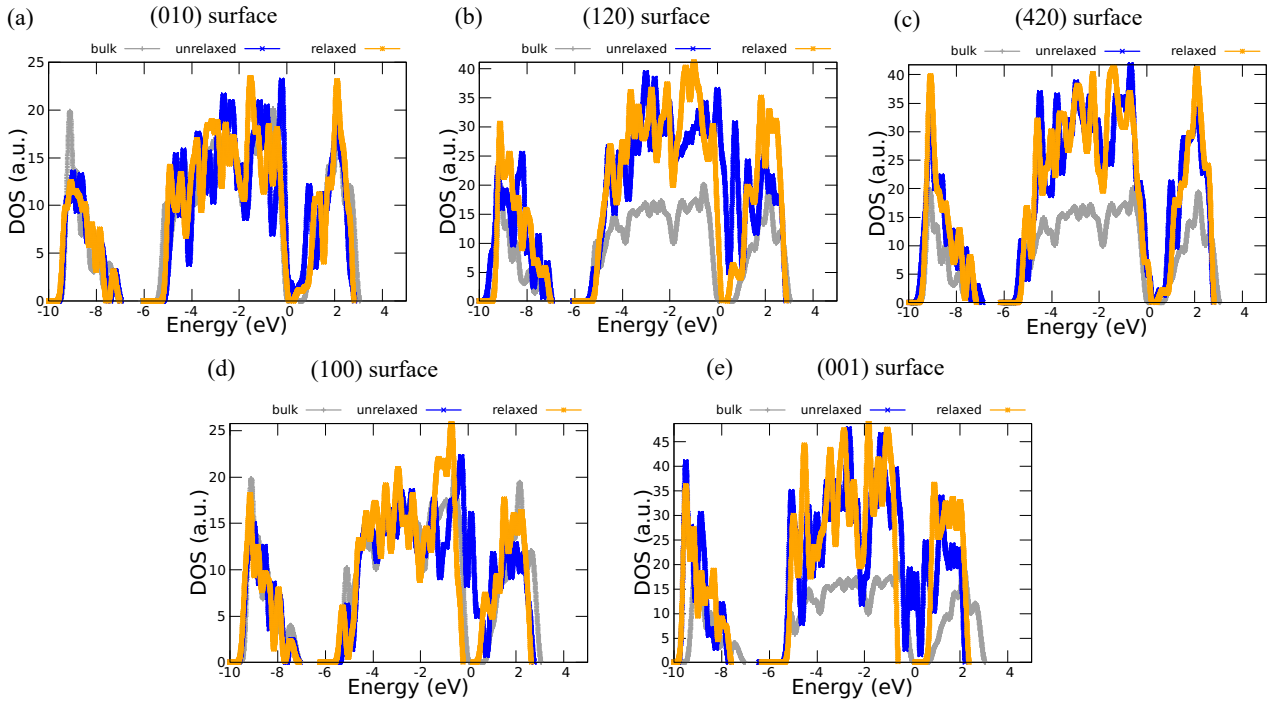

Figure 5.2: Density of states (DOS) of (a) (010) surface, (b) (120) surface, (c) (420) surface, (d) (100) surface, and (e) (001) surface.

1.20 Jm^{-2} for the unrelaxed surface and 0.64 Jm^{-2} for the optimized surface. The DOS plots in Figure 5.2 (d) and (e) gave insight on the large surface energies for (100) and (001) surfaces. Initially, both surfaces have large DOS inside the band gap. The presence of periodic images and incomplete Sb-Se bonding for Sb_4Se_6 nanoribbons introduced dangling bonds. After relaxation, most of these gap states were removed, indicating the self-healing of electronic structure which could be beneficial for photovoltaic application.

5.2.2 Slab Model with Ribbons Titled Away from the Slab

Lastly, we tested surfaces with ribbons oriented at an angle to the slab. In several research studies, (211) and (221) oriented ribbons have been observed in the Sb_2Se_3 based solar cells [17, 18, 38, 50]. Here we would like to study these two surface slabs (211) and (221) for a microscopic understanding. As shown in Figure 5.3 (a)—(d), both surfaces have ribbons oriented at an angle to the slab. Before relaxation, the surface slabs contain broken Sb-Se bonds.

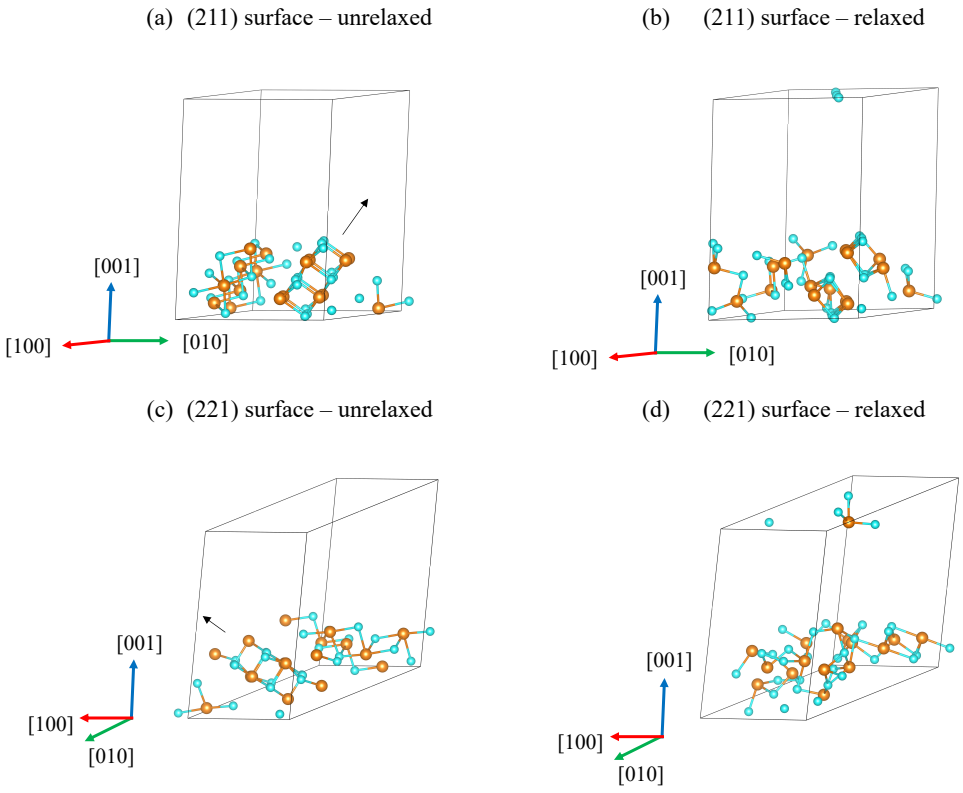

Figure 5.3: Unrelaxed and relaxed slabs of Sb_2Se_3 (a)—(b) (211) plane and (c)—(d) (221) plane. Black arrow indicates the direction of the ribbon.

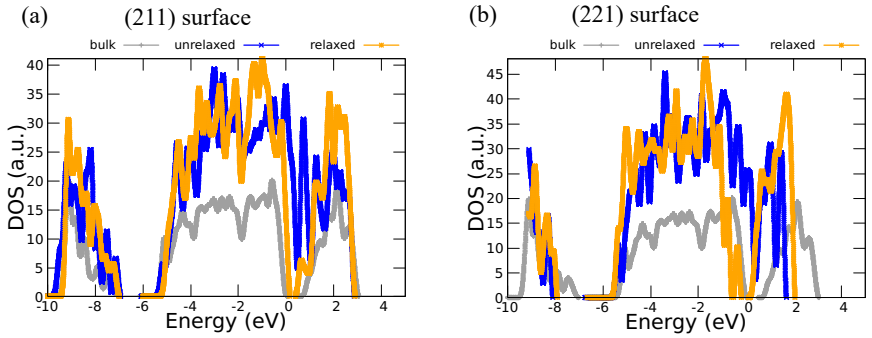

Figure 5.4: Density of states (DOS) of (a) (211) surface and (b) (221) surface.

After relaxation, most of the dangling bonds were reconstructed and formed new covalent bonds. However, both unrelaxed surfaces have high surface energy. For (211) surface, the surface energy is 1.84 Jm^{-2} for the unrelaxed one and 0.95 Jm^{-2} for the fully optimized one. For (221)

surface, the surface energy is slightly lower: 1.04 Jm^{-2} for the unrelaxed surface and 0.48 Jm^{-2} for the fully optimized surface. The DOS plots in Figure 5.4 (a) and (b) showed large gap states prior to relaxation. The gap states were reduced after relaxation, however unlike the previous surfaces, the gap states here did not completely disappear. These residual gap states could serve as recombination and scattering centers, which will be detrimental to the overall performance of the Sb_2Se_3 thin-film solar cell.

5.3 Conclusion

For highly anisotropic materials, surface termination can play a vital role. Mitigating the dangling bonds and removing the gap states will benefit the performance of solar cells, especially the surface terminations at the grain boundaries are benign. Due to its low structural dimensionality, ribbon-like chalcogenide materials such as Sb_2Se_3 have different surface energies for different cleaved surfaces. The vdW character allows the ribbons to form benign vdW bonds near the surface. Our results showed that cleaving a surface with Sb_4Se_6 ribbons parallel to the surface will create benign surfaces with low formation energies and minimal gap states. In addition, all surfaces were able to heal most of the dangling bonds after the structural relaxation, highlighting Sb_2Se_3's ability to self-heal the dangling bonds upon cleaving, although some of the surfaces still have a small amount of gap states. The results indicated that Sb_2Se_3 grains with vdW terminated surfaces are free of dangling bonds, beneficial to the photovoltaic performance.

6. STRAIN ENGINEERING OF ANTIMONY SELENIDE NANORIBBONS

6.1 Computational Approach

Strain engineering offers a viable approach to tune the bandgap of materials and control their electronic properties, especially in low-dimensional materials. Here we use strain engineering to modify the electronic structure of 1D $(Sb_4Se_6)_n$ nanoribbon. Specifically, we apply uniaxial tensile strain and uniaxial compressive strain along the ribbon direction, as seen in Figure 6.1. A large separation along *a*- and *b*- directions (> 13 Å) is included, followed by structural relaxation with a maximum residual force less than 0.02 eV/Å, self-consistent calculations, and band structure and DOS calculations, respectively. The energy in the band structures and DOS plots was shifted with respect to the vacuum level.

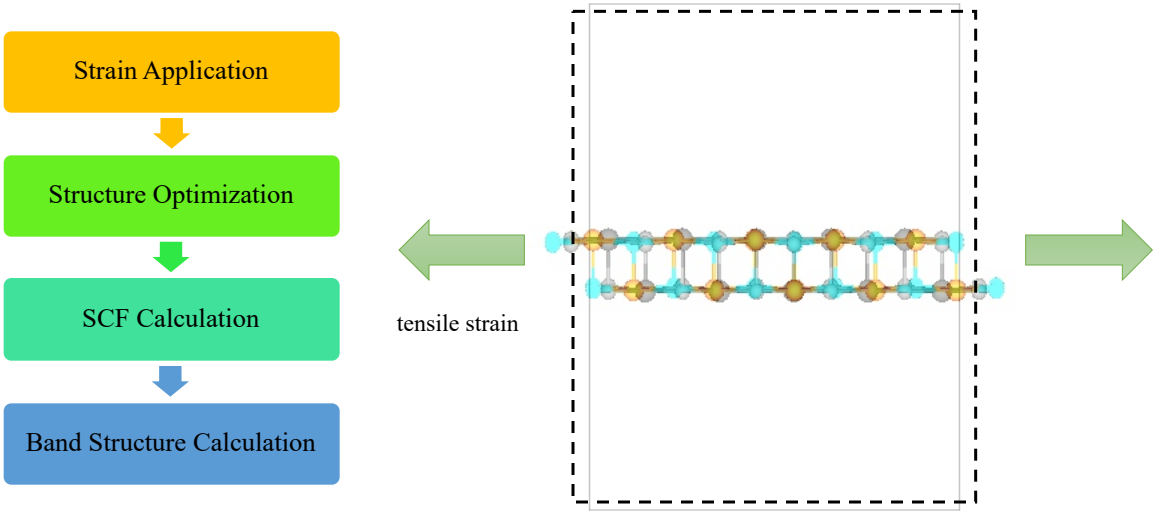

Figure 6.1: Schematic flow of strain-dependent electronic structure calculations. This process was applied to the tensile strain, compressive strain, and ripple studies.

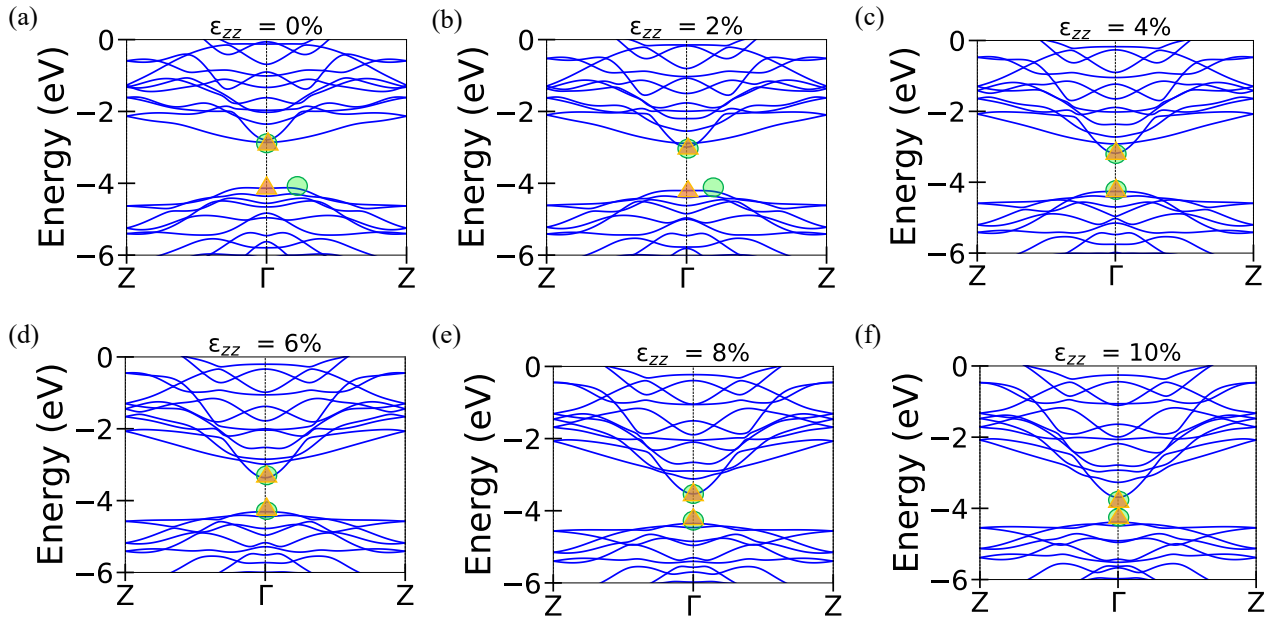

Figure 6.2: Band structures of 1D $(Sb_4Se_6)_n$ nanoribbons under different uniaxial tensile strains. The green circles indicate the VBM and CBM, while the orange triangles show the direct gap of each band structure.

6.1.1 Uniaxial Tensile Strain

The band structures in Figure 6.2 (a)–(f) show a gradual decrease in the band gap as the uniaxial tensile strain increases. For the unstrained ribbons with $\epsilon_{zz} = 0\%$ and $\epsilon_{zz} = 2\%$, an indirect bandgap is observed with the conduction band minimum (CBM) at the Γ point and the valence band maximum (VBM) on the ΓZ path. The CBM is significantly lowered as tensile strain is increased.

The direct gap remained at the Γ point for all strain values. Interestingly, the transition from indirect to direct gap was observed as VBM approaches the Γ point in $\epsilon_{zz} = 4\%$. After the transition, increasing the strain greatly reduced the band gap.

There is also a flattening of the topmost valence bands upon higher and higher tensile strain. The flat valence bands can be attributed to weaker interactions between the orbitals near the VBM, leading to a more localized eigenstate. This is also evident in the partial distribution of density states (PDOS) plotted in Figure 6.3 (a)—(d) for 0%, 2%, 4%, and 10% as the band gap character

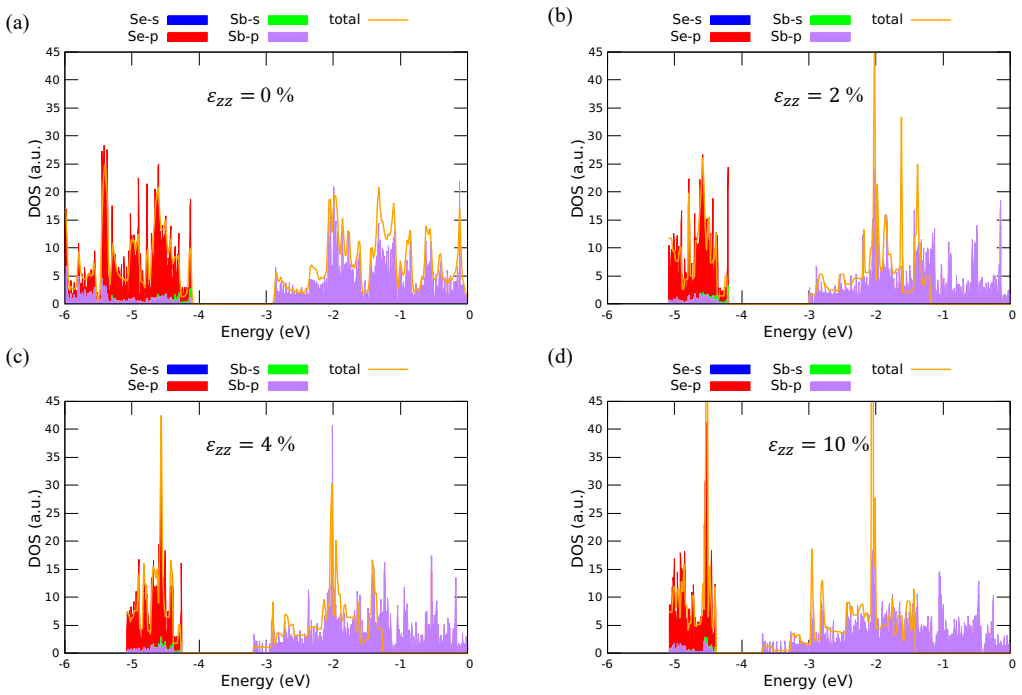

Figure 6.3: Projected DOS of 1D $(Sb_4Se_6)_n$ nanoribbons under different uniaxial tensile strains.

transitions from indirect to direct gap. For all tensile strains, Se *p* orbitals (red peaks) mostly occupied valence bands while Sb *p* orbitals (purple peaks) dominated conduction bands. The hybridization of Se *p* orbitals was gradually reduced with increasing tensile strain, as a result, the bands become more flattened.

The Sb *p* orbitals dominating VBM significantly shifted to the left, lowering the VBM and reducing the band gap. The band gap reduction is evident with the small peaks seen at -3.5 eV to -3 eV, which were previously unseen in the unstrained ribbon. This can be attributed to the change in Sb-Se bond length as the ribbon was pulled apart. The Sb-Se bond along the ribbon direction becomes longer while the Sb-Se bond orthogonal to the *c*- direction becomes shorter, thus the *p* orbitals for Sb and Se atoms become more localized, resulting in a decreased band gap.

6.1.2 Compressive Strain

For compressive strain, a similar trend was seen in terms of band gap reduction as the compressive strain is increased, as indicated in the band structures in Figure 6.4 (a)—(f). However,

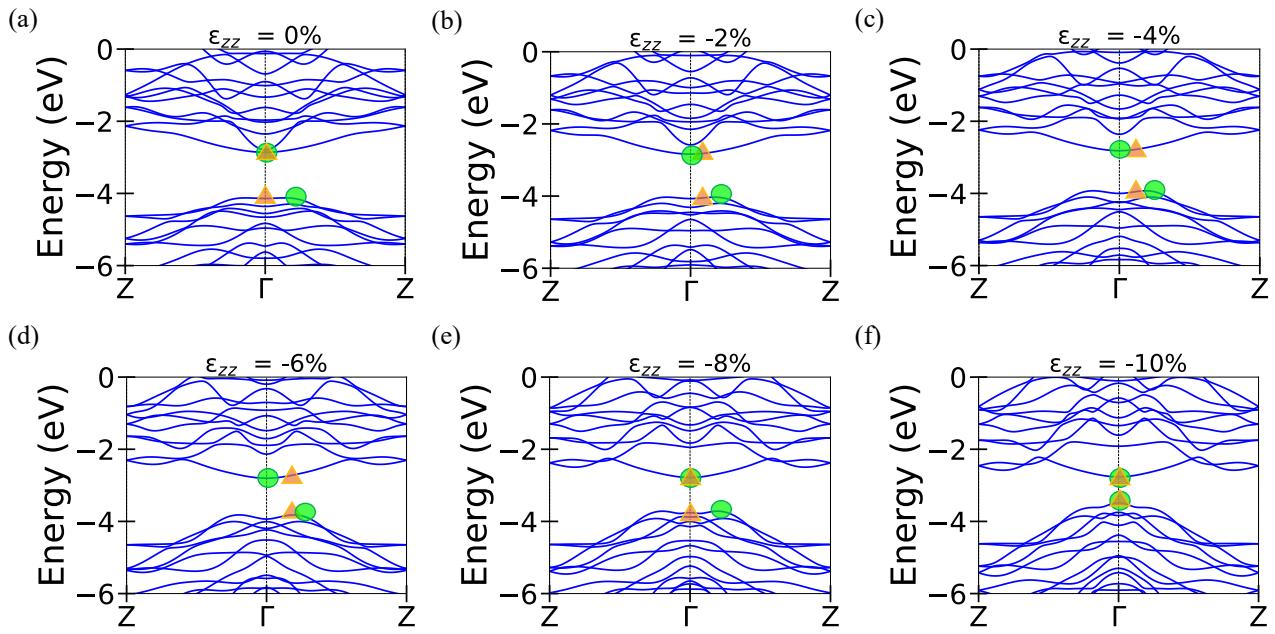

Figure 6.4: Band structures of 1D $(Sb_4Se_6)_n$ nanoribbons under different uniaxial compressive strains. The green circles indicate the VBM and CBM, while the orange triangles show the direct gap of each band structure.

we observed an upshift of VBM and a significant decrease of the gap. Initially, the direct gap is found at the Γ point. But as the ribbon was compressed, the direct gap started shifting towards the Z point. At $\epsilon_{zz} = -8\%$, the direct gap shifted back to the Γ point. The band gap transition only occurred at $\epsilon_{zz} = -10\%$ as the VBM shifted along the ΓZ path and towards Γ point. The shape of the valence bands (prominent curves) also suggested strong interaction between adjacent atomic orbitals near the VBM. The PDOS for 0%, -4%, -8%, and -10% were calculated, which were shown in Figure 6.5 (a)—(d). As ϵ_{zz} changes from -4% to -10%, we observed the increase of the VBM level and the localization of Se *p* orbitals near the VBM. The Sb *p* orbitals dominating CBM remains at the similar energy level, therefore the bandgap reduces.

The most notable aspect in both studies is the band gap reduction with increasing tensile and compressive strain. We studied the PDOS for $\epsilon_{zz} = 10\%$ and compared it with the unstrained ribbon, as shown in Figure 6.6 (a)—(c). The band gap between $\epsilon_{zz} = 10\%$ and $\epsilon_{zz} = -10\%$ are relatively close (0.02 eV difference), but the shift of VB and CB was different for each strain

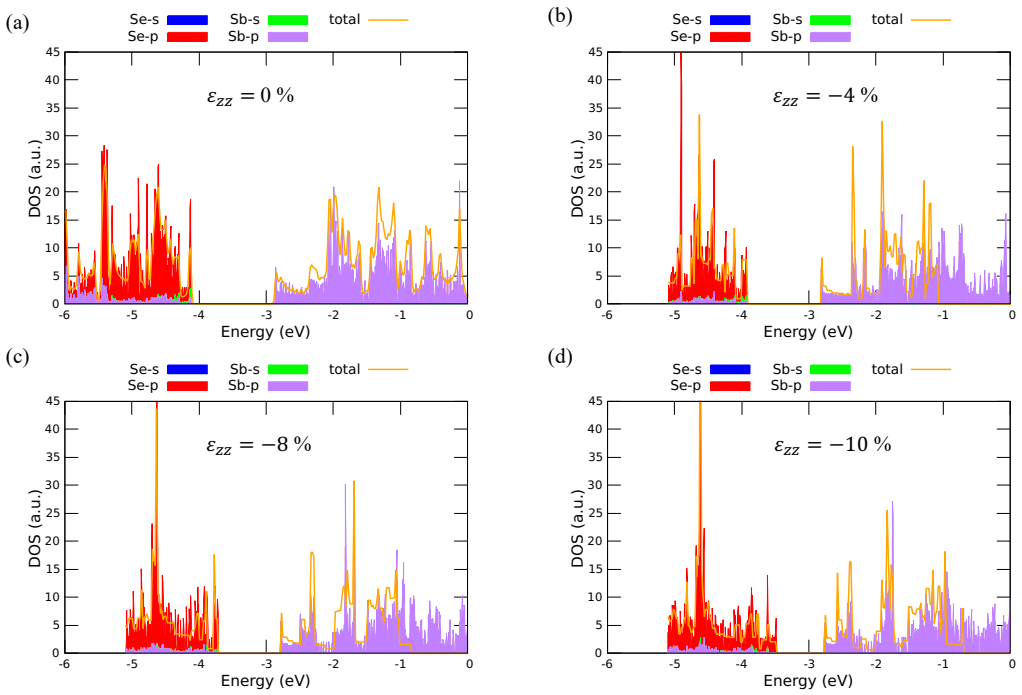

Figure 6.5: Projected DOS of 1D $(Sb_4Se_6)_n$ nanoribbons under different uniaxial compressive strains.

application. At tensile strain $\epsilon_{zz} = 10\%$, we observed a more localized Se *p* orbital in VB while CB was significantly lowered (shifted to the left). At compressive strain $\epsilon_{zz} = -10\%$, the Se *p* orbital in VB significantly increased in energy (shifted to the right).

The contrast in energy shifts was explained by the change in Sb-Se bond length along the ribbon direction and the transverse Sb-Se bond lengths. Tensile strain increased the bond length along *c*- direction, which greatly affected the electron orbital interaction between adjacent Sb and Se atoms. However, we observed the transverse Sb-Se bond lengths decreased by 0.05% which introduced some weakened interaction between adjacent orbitals in VB. The lowered CBM, mostly dominated by Sb *p* orbitals, can be attributed to the longer Sb-Se bonds along the ribbon direction.

Compressive strain decreased the bond length along the *c*- direction. As the ribbon is squeezed along its axis, the Sb-Se bond along the ribbon direction becomes shorter, which then induces stronger interaction between the *p* orbitals of Sb and Se, thereby causing the upshift of VB. The comparison between direct and indirect band gaps under compressive and tensile strain is shown

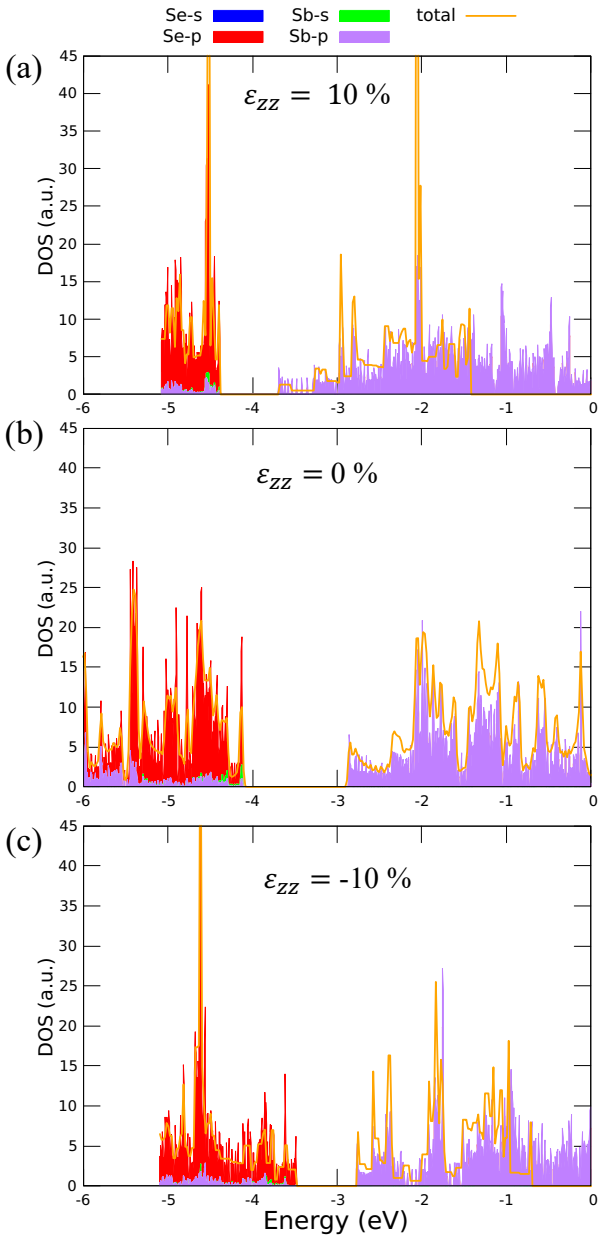

Figure 6.6: Comparison of PDOS of 1D $(Sb_4Se_6)_n$ nanoribbon under strain loading $\epsilon_{zz} = \pm 10\%$ and unstrained nanoribbon.

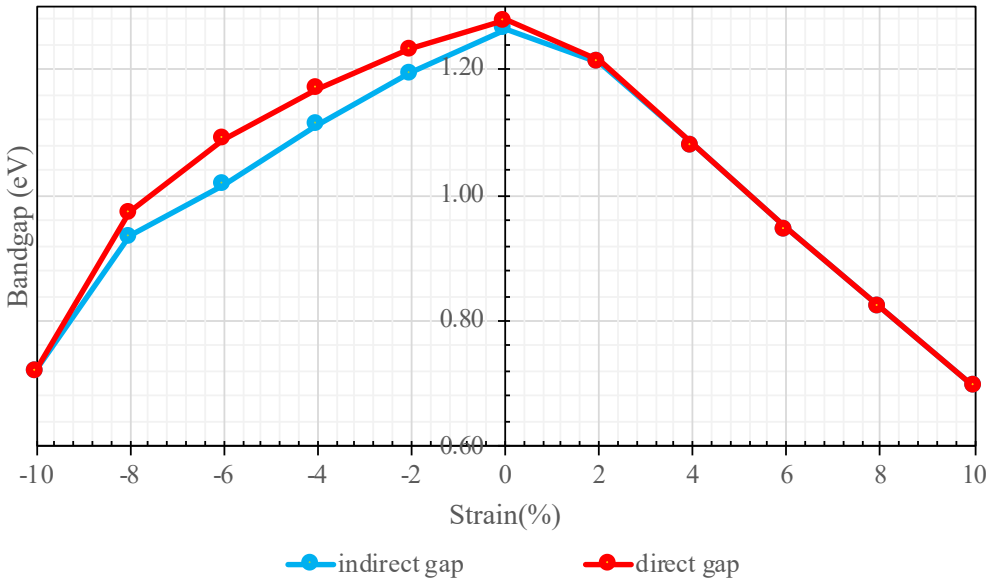

Figure 6.7: Comparison of band gap under uniaxial tensile and compressive strain. The values in bold indicate the band gap transition from indirect to direct gap. For tensile strain, gap transition occurred at $\epsilon_{zz} = 4\%$, while the transition from compressive strain occurred at $\epsilon_{zz} = -10\%$.

in Figure 6.7.

6.2 Conclusion

Strain engineering is shown to be a viable approach in tuning the band gap of 1D $(Sb_4Se_6)_n$ nanoribbons. Band gap decreases with increasing uniaxial tensile and compressive strain. However, the indirect-to-direct band gap transition occurs at lower tensile strain than compressive strain. Tensile strain led to a decrease of the CBM level, while compressive strain caused an increase of the VBM level, which is due to the decreased/increased orbital interactions as the bond length increases/decreases.

7. RIPPLE STRUCTURE

7.1 Introduction

For low-dimensional materials, the flexural modes can lead to the emergence of ripples/wrinkles when they are subject to compressive strain. In fact, ripple was found to form spontaneously in free-standing 2D materials such as graphene [1, 51] and MoS_2 [4, 5, 6, 13, 51, 52] after mechanical exfoliation of ultra-thin monolayers. Ripples and wrinkles can also affect the underlying electronic structure. Here, we would like to study the ripples in 1D $(Sb_4Se_6)_n$ nanoribbon and investigate the effect of ripples in the electronic structure.

7.2 Application of Ripples in Antimony Selenide Nanoribbon Supercell

We constructed the ripple by applying a periodic sinusoidal displacement along the b-direction, as shown in Figure 7.1. The displacement was described by a simple sine function:

$$\Delta y = A\sin(2\pi nz + \varphi)$$

where A is the maximum vertical shift of the y-coordinates, n is the number of periods of the sine curve, and φ is the phase shift of the curve. For simplicity, we set a maximum displacement A of 1%, a minimum n value of 1, and no phase shift to simulate a general ripple scheme. We applied varying compressive strain to compare the deformation of the rippled ribbon after relaxation.

Uniaxial compressive load was applied on a supercell configuration of 60 atoms (1x1x6 unit cells) with a large separation along *a*- and *b*- directions (> 13 Å), followed by structural relaxation with the maximum residual force less than 0.02 eV/Å while maintaining the applied strain. Self-consistent calculations used a smaller plane-wave energy cutoff of 15 Ry and a Monkhorst-Pack k-point sampling grid of 1x1x3. Band structures and DOS plots were shifted with respect to vacuum level.

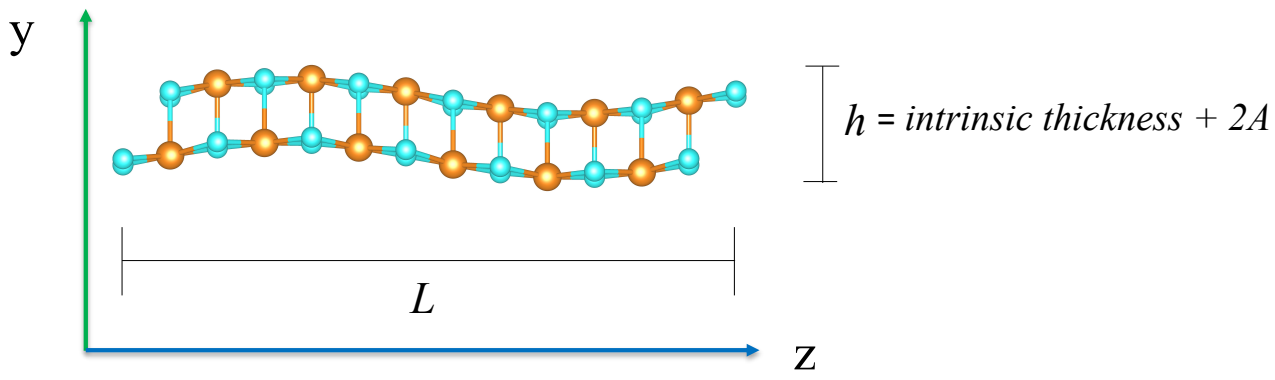

Figure 7.1: Initial rippled structure generated from the equation. h is the ripple height and L is the length of the nanoribbon.

Table 7.1: Maximum ribbon height h and length L of the ripple configurations. Initial h and L describe the initial ribbon configuration prior to adding the sinusoidal displacement to form the ripple structure.

ε_{zz}	h (Å)	L (Å)
unrippled	0.00	23.63
-5%	0.02	22.44
-7%	3.81	21.97
-8%	4.63	21.74
-10%	5.29	21.26
-12%	6.28	20.79

7.3 Ripple Structure Optimization

Figure 7.2 (a)—(e) illustrate the curvature difference for rippled ribbons under various compressive strains before and after relaxation.

After structural relaxation, we observed an increase in the ripple height h with increasing compressive strain, as shown in Figure 7.2 (b)—(e). Interestingly, the pre-constructed ripples for ϵ_{zz}=-

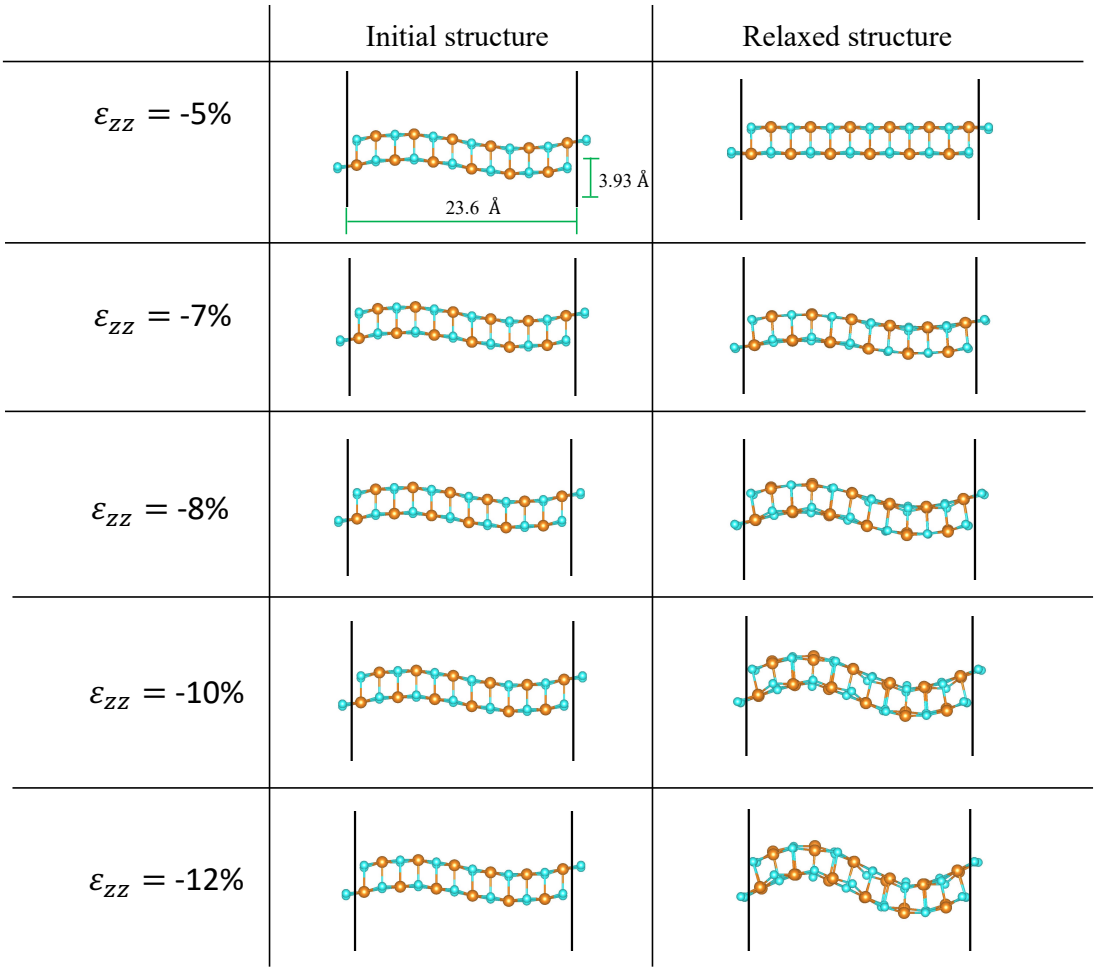

Figure 7.2: Initial and relaxed rippled $(Sb_4Se_6)_n$ nanoribbons with varying compressive strain. Sb: orange, and Se: blue.

5% was relaxed back to a ripple-free structure, indicating the in-plane stress at this stage is not enough to effectively induce an out-of-plane deformation. Bond length reduction was sufficient to compensate for the structure deformation after relaxation, but a longer ribbon chain may generate a ripple formation after relaxation. The ripple slowly emerged with larger compression loading, as shown Figure 7.3 (a) and (b). Ripple height *h* and ribbon length *L* are listed in Table 7.1.

7.4 Band Structure

The band structures for the compressive strain values were plotted in Figure 7.4, which shows that the band gap decreases for the rippled nanoribbons under increasing compressive strain. For

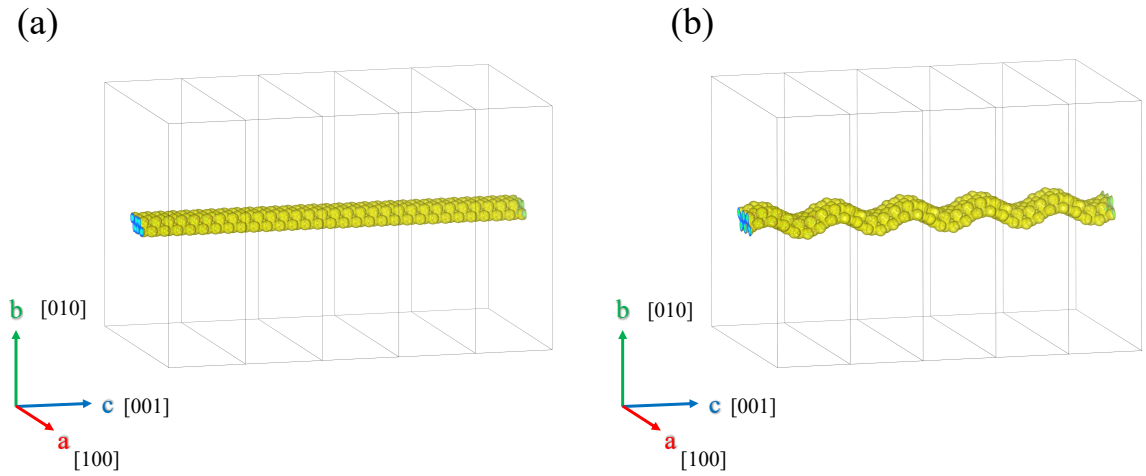

Figure 7.3: Isosurface charge density plot for (a) $\epsilon_{zz} = -5\%$ and (b) $\epsilon_{zz} = -12\%$ relaxed rippled ribbons in the supercell.

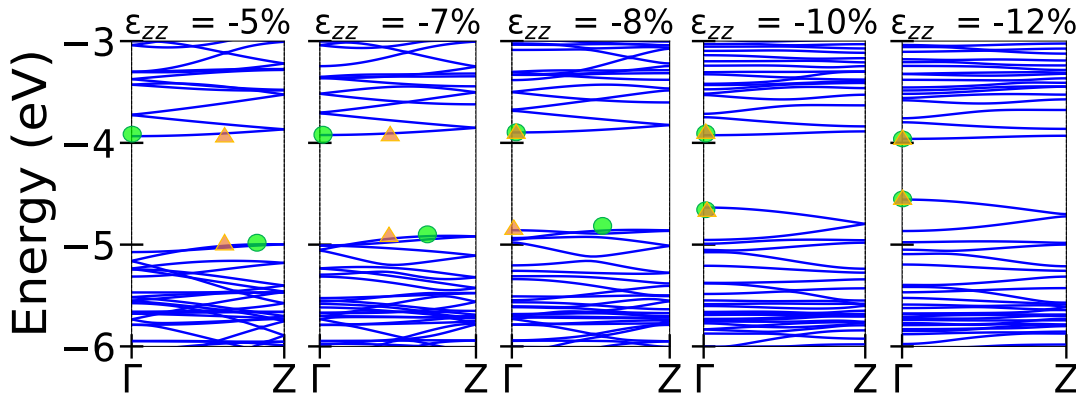

Figure 7.4: Band structures of rippled 1D $(Sb_4Se_6)_n$ nanoribbons under different uniaxial compressive strains. The green circles indicate the VBM and CBM, while the orange triangles show the direct gap of each band structure.

rippled ribbons under compressive strain of $\epsilon_{zz} = -5\%$ to $\epsilon_{zz} = -8\%$, the indirect band gap is located at the CBM at the Γ point and the VBM on the ΓZ path. The direct gap initially on the ΓZ path slowly shifted back to Γ point as the compression increases. Indirect-to-direct band gap transition occurred at $\epsilon_{zz} = -10\%$. Further compression to $\epsilon_{zz} = -12\%$ decreased the direct band gap from 0.71 eV to 0.60 eV.

7.5 Conclusion

In summary, the results showed the ripple structures affect the electronic structure with increasing compressive strain. We first constructed the ripple by applying a periodic sinusoidal displacement transverse to the ribbon axis, then applied compressive strain and optimized the rippled nanoribbon. The ripple height increases in the optimized 1D $(Sb_4Se_6)_n$ nanoribbons with increasing compressive strain, while the band gap decreases. The indirect-to-direct gap transition occurred at a higher compressive strain, which may lead to a drastic change in the photoluminescence.

8. SUMMARY AND OUTLOOK

In summary, we performed a systematic study of atomic and electronic structure of bulk Sb_2Se_3 and 1D $(Sb_4Se_6)_n$ nanoribbon using first-principles DFT approach. Understanding the anisotropic nature of 1D $(Sb_4Se_6)_n$ nanoribbon and its strain-dependent electronic properties may shed light on the possibilities of achieving tunable band gap in the 1D semiconductors in future.

To achieve this goal, we first optimized the parameters for DFT calculations and benchmarked pseudopotentials plus vdW correction before performing band structure and density of state calculations of bulk Sb_2Se_3 and 1D $(Sb_4Se_6)_n$ nanoribbon. Band gap values for bulk Sb_2Se_3 was lower than the experimental band gap values which is expected for DFT with the GGA-PBE functional. Band dispersion is reduced 1D $(Sb_4Se_6)_n$ nanoribbon due to the absence of interchain vdW interaction, leading to a widening in band gap. Surface termination studies further elucidated the cohesive energy calculations by considering cleaving planes and ensuring the cleaved slab is benign at the grain boundaries. The vdW character not only provides a flexible surface structure, but also prevents the dangling bonds at the surface. The absence of dangling bonds at the surfaces of Sb_2Se_3 grains may potentially benefit the photovoltaic performance. vdW terminated surfaces have reduced dangling bonds and reduce the recombination centers of photoexcited electron and holes in photovoltaics.

Strain engineering proved a viable solution in tuning the band gap of 1D $(Sb_4Se_6)_n$ nanoribbon. Both uniaxial tensile and compressive strain lead to the decrease in the band gap with increasing strain. An indirect-to-direct band gap transition occurs in both tensile strain and compressive strain. Our findings suggest that elastic strain engineering may be useful to tune the electronic structure of other 1D nanoribbons.

We further studied the ripple structure of 1D $(Sb_4Se_6)_n$ nanoribbon. The calculated electronic band structures showed that the band gap of the rippled $(Sb_4Se_6)_n$ nanoribbon decreases under increasing compressive strain. Thus, compressive stress can generate ripple structures in the 1D nanoribbons and significantly change their electronic structure, *e.g.* forming localized photon emis-

sion centers at the tip of the ripple, potentially useful for providing single photon source. Our findings suggest ripple engineering as a potential route to tune the electronic structure of nanoribbons for straintronic applications.

REFERENCES

[1] W. Bao, F. Miao, Z. Chen, H. Zhang, W. Jang, C. Dames, and C. N. Lau, "Controlled ripple texturing of suspended graphene and ultrathin graphite membranes," *Nature Nanotechnology*, vol. 4, no. 9, pp. 562–566, 2009.

[2] C. R. Dean, A. F. Young, I. Meric, C. Lee, L. Wang, S. Sorgenfrei, K. Watanabe, T. Taniguchi, P. Kim, K. L. Shepard, and J. Hone, "Boron nitride substrates for high-quality graphene electronics," *Nature Nanotechnology*, vol. 5, no. 10, pp. 722–726, 2010.

[3] J. Qi, X. Qian, L. Qi, J. Feng, D. Shi, and J. Li, "Strain-engineering of band gaps in piezoelectric boron nitride nanoribbons," *Nano Letters*, vol. 12, no. 3, pp. 1224–1228, 2012.

[4] K. F. Mak, C. Lee, J. Hone, J. Shan, and T. F. Heinz, "Atomically thin mos2: A new direct-gap semiconductor," *Physical Review Letters*, vol. 105, no. 13, p. 136805, 2010.

[5] H. J. Conley, B. Wang, J. I. Ziegler, R. F. Haglund, S. T. Pantelides, and K. I. Bolotin, "Bandgap engineering of strained monolayer and bilayer mos2," *Nano Letters*, vol. 13, no. 8, pp. 3626–3630, 2013.

[6] P. Miró, M. Ghorbani-Asl, and T. Heine, "Spontaneous ripple formation in mos2 monolayers: Electronic structure and transport effects," *Advanced Materials*, vol. 25, no. 38, pp. 5473–5475, 2013.

[7] G. Lu, K. Yu, Z. Wen, and J. Chen, "Semiconducting graphene: converting graphene from semimetal to semiconductor," *Nanoscale*, vol. 5, no. 4, pp. 1353–1368, 2013.

[8] X. Zhang, O. V. Yazyev, J. Feng, L. Xie, C. Tao, Y.-C. Chen, L. Jiao, Z. Pedramrazi, A. Zettl, S. G. Louie, H. Dai, and M. F. Crommie, "Experimentally engineering the edge termination of graphene nanoribbons," *ACS Nano*, vol. 7, no. 1, pp. 198–202, 2013.

[9] S. Deng and V. Berry, "Wrinkled, rippled and crumpled graphene: an overview of formation mechanism, electronic properties, and applications," *Materials Today*, vol. 19, no. 4, pp. 197–

212, 2016.

[10] C. Shuai, B. Wang, Y. Yang, S. Peng, and C. Gao, "3d honeycomb nanostructure-encapsulated magnesium alloys with superior corrosion resistance and mechanical properties," *Composites Part B: Engineering*, vol. 162, pp. 611–620, 2019.

[11] Q. Tang, Y. Cui, Y. Li, Z. Zhou, and Z. Chen, "How do surface and edge effects alter the electronic properties of gan nanoribbons?," *The Journal of Physical Chemistry C*, vol. 115, no. 5, pp. 1724–1731, 2011.

[12] E. D. Minot, Y. Yaish, V. Sazonova, J.-Y. Park, M. Brink, and P. L. McEuen, "Tuning carbon nanotube band gaps with strain," *Physical Review Letters*, vol. 90, no. 15, p. 156401, 2003.

[13] J. Qi, X. Li, X. Qian, and J. Feng, "Bandgap engineering of rippled mos2 monolayer under external electric field," *Applied Physics Letters*, vol. 102, no. 17, p. 173112, 2013.

[14] H. Koc, A. M. Mamedov, E. Deligoz, and H. Ozisik, "First principles prediction of the elastic, electronic, and optical properties of sb2s3 and sb2se3 compounds," *Solid State Sciences*, vol. 14, no. 8, pp. 1211–1220, 2012.

[15] M. R. Filip, C. E. Patrick, and F. Giustino, "Gw quasiparticle band structures of stibnite, antimonselite, bismuthinite, and guanajuatite," *Physical Review B*, vol. 87, no. 20, p. 205125, 2013.

[16] H. Song, T. Li, J. Zhang, Y. Zhou, J. Luo, C. Chen, B. Yang, C. Ge, Y. Wu, and J. Tang, "Highly anisotropic sb2se3 nanosheets: Gentle exfoliation from the bulk precursors possessing 1d crystal structure," *Advanced Materials*, vol. 29, no. 29, p. 1700441, 2017.

[17] L. Guo, B. Zhang, Y. Qin, D. Li, L. Li, X. Qian, and F. Yan, "Tunable quasi-one-dimensional ribbon enhanced light absorption in sb2se3 thin-film solar cells grown by close-space sublimation," *Solar RRL*, vol. 2, no. 10, p. 1800128, 2018.

[18] Y. Zhou, L. Wang, S. Chen, S. Qin, X. Liu, J. Chen, D.-J. Xue, M. Luo, Y. Cao, Y. Cheng, E. H. Sargent, and J. Tang, "Thin-film sb2se3 photovoltaics with oriented one-dimensional ribbons and benign grain boundaries," *Nature Photonics*, vol. 9, no. 6, pp. 409–415, 2015.

[19] J. Kim, W. Yang, Y. Oh, H. Lee, S. Lee, H. Shin, J. Kim, and J. Moon, "Self-oriented sb2se3 nanoneedle photocathodes for water splitting obtained by a simple spin-coating method," *J. Mater. Chem. A*, vol. 5, pp. 2180–2187, 2017.

[20] W. Kohn and L. J. Sham, "Self-consistent equations including exchange and correlation effects," *Physical Review*, vol. 140, no. 4A, pp. A1133–A1138, 1965.

[21] P. Hohenberg and W. Kohn, "Inhomogeneous electron gas," *Physical Review*, vol. 136, no. 3B, pp. B864–B871, 1964.

[22] J. P. Perdew and A. Zunger, "Self-interaction correction to density-functional approximations for many-electron systems," *Physical Review B*, vol. 23, no. 10, pp. 5048–5079, 1981.

[23] J. P. Perdew, K. Burke, and M. Ernzerhof, "Generalized gradient approximation made simple," *Physical Review Letters*, vol. 77, no. 18, pp. 3865–3868, 1996.

[24] V. Barone, M. Casarin, D. Forrer, M. Pavone, M. Sambi, and A. Vittadini, "Role and effective treatment of dispersive forces in materials: Polyethylene and graphite crystals as test cases," *Journal of Computational Chemistry*, vol. 30, no. 6, pp. 934–939, 2009.

[25] S. Grimme, S. Ehrlich, and L. Goerigk, "Effect of the damping function in dispersion corrected density functional theory," *Journal of Computational Chemistry*, vol. 32, no. 7, pp. 1456–1465, 2011.

[26] S. Grimme, J. Antony, S. Ehrlich, and H. Krieg, "A consistent and accurate ab initio parametrization of density functional dispersion correction (dft-d) for the 94 elements h-pu," *The Journal of Chemical Physics*, vol. 132, no. 15, p. 154104, 2010.

[27] J. Vackář, M. Hyt'ha, and A. Šimůnek, "All-electron pseudopotentials," *Physical Review B*, vol. 58, no. 19, pp. 12712–12720, 1998.

[28] J. Lee, *Computational Materials Science: An Introduction, Second Edition*. CRC Press, 2nd ed., 2016.

[29] D. R. Hamann, M. Schlüter, and C. Chiang, "Norm-conserving pseudopotentials," *Physical Review Letters*, vol. 43, no. 20, pp. 1494–1497, 1979.

[30] D. Vanderbilt, "Soft self-consistent pseudopotentials in a generalized eigenvalue formalism," *Physical Review B*, vol. 41, no. 11, pp. 7892–7895, 1990.

[31] P. E. Blöchl, "Projector augmented-wave method," *Physical Review B*, vol. 50, no. 24, pp. 17953–17979, 1994.

[32] P. Giannozzi, O. Andreussi, T. Brumme, O. Bunau, M. Buongiorno Nardelli, M. Calandra, R. Car, C. Cavazzoni, D. Ceresoli, M. Cococcioni, N. Colonna, I. Carnimeo, A. Dal Corso, S. de Gironcoli, P. Delugas, R. A. DiStasio, A. Ferretti, A. Floris, G. Fratesi, G. Fugallo, R. Gebauer, U. Gerstmann, F. Giustino, T. Gorni, J. Jia, M. Kawamura, H. Y. Ko, A. Kokalj, E. Küçükbenli, M. Lazzeri, M. Marsili, N. Marzari, F. Mauri, N. L. Nguyen, H. V. Nguyen, A. Otero-de-la Roza, L. Paulatto, S. Poncé, D. Rocca, R. Sabatini, B. Santra, M. Schlipf, A. P. Seitsonen, A. Smogunov, I. Timrov, T. Thonhauser, P. Umari, N. Vast, X. Wu, and S. Baroni, "Advanced capabilities for materials modelling with quantum espresso," *Journal of Physics: Condensed Matter*, vol. 29, no. 46, p. 465901, 2017.

[33] P. Giannozzi, S. Baroni, N. Bonini, M. Calandra, R. Car, C. Cavazzoni, D. Ceresoli, G. L. Chiarotti, M. Cococcioni, I. Dabo, A. Dal Corso, S. de Gironcoli, S. Fabris, G. Fratesi, R. Gebauer, U. Gerstmann, C. Gougoussis, A. Kokalj, M. Lazzeri, L. Martin-Samos, N. Marzari, F. Mauri, R. Mazzarello, S. Paolini, A. Pasquarello, L. Paulatto, C. Sbraccia, S. Scandolo, G. Sclauzero, A. P. Seitsonen, A. Smogunov, P. Umari, and R. M. Wentzcovitch, "Quantum espresso: a modular and open-source software project for quantum simulations of materials," *Journal of Physics: Condensed Matter*, vol. 21, no. 39, p. 395502, 2009.

[34] P. Giannozzi, O. Baseggio, P. Bonfà, D. Brunato, R. Car, I. Carnimeo, C. Cavazzoni, S. d. Gironcoli, P. Delugas, F. F. Ruffino, A. Ferretti, N. Marzari, I. Timrov, A. Urru, and S. Baroni, "Quantum espresso toward the exascale," *The Journal of Chemical Physics*, vol. 152, no. 15, p. 154105, 2020.

[35] N. Kuganathan, "Antimony selenide crystals encapsulated within single walled carbon nanotubes-a dft study," *E-Journal of Chemistry*, vol. 6, p. 837807, 2009.

[36] W. Liu, X. Peng, C. Tang, L. Sun, K. Zhang, and J. Zhong, "Anisotropic interactions and strain-induced topological phase transition in sb2se3 and bi2se3," *Physical Review B*, vol. 84, no. 24, p. 245105, 2011.

[37] B. Tuttle, S. Alhassan, and S. Pantelides, "Computational predictions for single chain chalcogenide-based one-dimensional materials," *Nanomaterials (Basel, Switzerland)*, vol. 7, no. 5, p. 115, 2017.

[38] K. P. McKenna, "Self-healing of broken bonds and deep gap states in sb2se3 and sb2s3," *Advanced Electronic Materials*, vol. 7, no. 3, p. 2000908, 2021.

[39] N. Troullier and J. L. Martins, "Efficient pseudopotentials for plane-wave calculations," *Physical Review B*, vol. 43, no. 3, pp. 1993–2006, 1991.

[40] S. Grimme, "Semiempirical gga-type density functional constructed with a long-range dispersion correction," *Journal of Computational Chemistry*, vol. 27, no. 15, pp. 1787–1799, 2006.

[41] E. A. El-Sayad, A. M. Moustafa, and S. Y. Marzouk, "Effect of heat treatment on the structural and optical properties of amorphous sb2se3 and sb2se2s thin films," *Physica B: Condensed Matter*, vol. 404, no. 8, pp. 1119–1127, 2009.

[42] X. Ou, C. Yang, X. Xiong, F. Zheng, Q. Pan, C. Jin, M. Liu, and K. Huang, "A new rgo-overcoated sb2se3 nanorods anode for na+ battery: In situ x-ray diffraction study on a live sodiation/desodiation process," *Advanced Functional Materials*, vol. 27, no. 13, p. 1606242, 2017.

[43] C. Wood, Z. Hurych, and J. C. Shaffer, "Optical and transport properties of amorphous sb2se3," *Journal of Non-Crystalline Solids*, vol. 8-10, pp. 209–214, 1972.

[44] I. Levin, "Nist inorganic crystal structure database (icsd)," 2020.

[45] M. C. Payne, M. P. Teter, D. C. Allan, T. A. Arias, and J. D. Joannopoulos, "Iterative minimization techniques for ab initio total-energy calculations: molecular dynamics and conjugate gradients," *Reviews of Modern Physics*, vol. 64, no. 4, pp. 1045–1097, 1992.

[46] Y. Hinuma, G. Pizzi, Y. Kumagai, F. Oba, and I. Tanaka, "Band structure diagram paths based on crystallography," *Computational Materials Science*, vol. 128, pp. 140–184, 2017.

[47] A. Togo and I. Tanaka, "Spglib: a software library for crystal symmetry search," *arXiv: Materials Science*, 2018.

[48] A. Kokalj, "Computer graphics and graphical user interfaces as tools in simulations of matter at the atomic scale," *Computational Materials Science*, vol. 28, no. 2, pp. 155–168, 2003.

[49] W. Sun and G. Ceder, "Efficient creation and convergence of surface slabs," *Surface Science*, vol. 617, pp. 53–59, 2013.

[50] Z. Li, X. Liang, G. Li, H. Liu, H. Zhang, J. Guo, J. Chen, K. Shen, X. San, W. Yu, R. E. I. Schropp, and Y. Mai, "9.2%-efficient core-shell structured antimony selenide nanorod array solar cells," *Nature Communications*, vol. 10, no. 1, p. 125, 2019.

[51] J. C. Meyer, A. K. Geim, M. I. Katsnelson, K. S. Novoselov, T. J. Booth, and S. Roth, "The structure of suspended graphene sheets," *Nature*, vol. 446, no. 7131, pp. 60–63, 2007.

[52] J. Brivio, D. T. L. Alexander, and A. Kis, "Ripples and layers in ultrathin mos2 membranes," *Nano Letters*, vol. 11, no. 12, pp. 5148–5153, 2011.